RF Coils Design for Small Animal MRI Lung Imaging at 3T Using Hyperpolarized ^{129}Xe and Inert Fluorinated Gases

by

Tao Li

A thesis submitted to the faculty of graduate studies
in partial fulfillment of the requirements for the degree of
Masters of Science in Electrical and Computer Engineering

Department of Engineering
Lakehead University

Thunder Bay, Ontario, Canada
July 16th, 2013

ABSTRACT

This thesis described the investigation, construction and testing of two sets of RF coils for their applications in novel lung MRI imaging techniques.

In the first part of the thesis, a quadrature-driven birdcage coil for rat lung MRI using inert fluorinated gases was developed. Methods for coil tuning and impedance matching were presented and discussed. The sensitivity improvement resulted from a quadrature-driven mode was quantitatively measured, and compared to the linear reference. A dual-angle method (DAM) was studied and implemented to quantitatively measure the B_1 field homogeneity, and a B_1 field map was generated at the center of the coil. *In vivo* rat lung imaging experiments were conducted using the constructed coil, and the multi-slice images acquired from the rat lung were presented.

In the second part of the thesis, a ^{1}H-^{129}Xe double-birdcage coil for rat lung MRI using hyperpolarized 129Xe gas was developed. The Q factors of each coil was measured and compared before and after the double-birdcage structure was formed. The coupling between the two coils was tested, and a geometrical decoupling method was implemented and optimized. Imaging scans using thermal xenon phantom and saline syringe phantom were conducted with image registration post-processing performed, and the dual-frequency scan ability of the developed coil was verified and evaluated.

ACKNOWLEDGEMENT

Firstly, I would like to thank my co-supervisor Dr. Mitchell Albert, whose support, advice, accessibility and encouragement has been invaluable to me throughout my graduate study and thesis research. And I also would like to thank my supervisor Dr. Laura Curiel, for her continuous support and help.

I would like to express my sincerest gratitude to Mr. Ralph Hashoian (Clinical MR Solution, LLC), a great engineer and mentor, not only for his expert tutoring in RF knowledge, and generous sharing of many invaluable experiences in coil engineering, but also for his kind encouragement that inspires me to become a professional engineer.

Many thanks must go to Dr. Matthew Fox for his help in NMR theory and supports in animal experiments preparations. And I also would like to thank Mr. Marcus Couch for his help through my courses study.

I reserve my special thanks for Dr. Iain Ball, for our countless hours of Starbucks MRI talks, and his professional support that have greatly helped me in my study and research.

Finally, I am eternally grateful to my families for their never-end love and support.

TABLE OF CONTENTS

LIST OF FIGURES

LIST OF TABLES

LIST OF SYMBOLS

Symbol	Meaning
T	Tesla
^{129}Xe	Xenon – 129
^{19}F	Fluorine - 19
^{3}He	Helium - 3
^{1}H	Proton
I	Quantum number
M	Magnetization
h	Planck constant
γ	Gyromagnetic ratio
g	Lande g-factor
e	Charge of an electron
m	Mass
B_0	Main magnetic field
k_B	Boltzmann constant
B_1	Excitation magnetic field
α	Flip angle
T_1	Longitudinal relaxation time
T_2	Transverse relaxation time
J	Current density
E	Electric field
Q	Quality factor
Δf	3-db bandwidth
Γ	Reflection coefficient
χ	Susceptibility
η_f	Filling factor
μ_0	Permeability

LIST OF ABBREVIATIONS

Abbreviation	Meaning
NMR	Nuclear magnetic resonance
MRI	Magnetic resonance imaging
RF	Radio frequency
FID	Free induction decay
SNR	Signal to noise ratio
FOV	Field of view
ROI	Region of interest
PFP	Perfluoropropane
SV	Single voxel
TR	Repetition time
TE	Echo time
FFE	Fast field echo (pulse sequence)
DAM	Double angle method

CHAPTER 1 INTRODUCTION

1.1 Background

The phenomenon of Nuclear Magnetic Resonance (NMR) was firstly discovered by Purcell [1] and Bloch [2] in 1946. In 1973, Lauterbur [3] and Mansfield [4] developed the techniques to generate images of a subject from NMR signals using Fourier Transform. Ever since then, magnetic resonance imaging (MRI) technique has been rapidly developed and has become one of the most valuable and widely-used diagnostic imaging modalities. This non-invasive diagnostic imaging technique has the ability to provide tomography images with structural information of an interested region of the human body. In addition, the development of functional MRI (fMRI) has made it an essential research tool in psychology and physiology, providing not only the structural, but also functional information of the human brain.

Nevertheless, there are important tissues and organs in the human body that resist the conventional MRI techniques, such as the lungs, to name one. This is because the conventional MRI technique adopts proton (^{1}H) as the imaging contrast for its abundance in human body. However, the proton density in the lungs is very low due to the vast cavity inside, which drastically limits the NMR signal strength from generating images of diagnostic values. Besides, the micro structures of the bronchus and alveolar create countless interfaces between the lung tissues and the air, and result in a very inhomogeneous susceptibility and thus a distorted field distribution. This further handicapped the conventional MRI from generating useful lung images.

In 1994, Albert *et al*. [5] developed a novel technique using hyperpolarized novel gases as imaging contrasts to image the lungs with MRI techniques. In this technique, hyperpolarization of the noble gas nuclei (^{3}He, ^{129}Xe) is achieved by either spin exchange with optically pumped rubidium atoms (SEOP), or metastability exchange optical pumping (MEOP), and the signal intensity from the hyperpolarized nuclei can be increased up to a hundred thousand times. Hyperpolarized noble gas MRI has shown dramatic results for imaging of the lungs, and proven to be an effective method for evaluating, and staging the progress of treatment of, pulmonary diseases.

On the other hand, Kuethe *et al.* has demonstrated the first use of inert fluorinated MRI 15 years ago[6]. And recently Soher *et al.* [7] has shown another approach to MRI lung imaging using inert fluorinated gases, such as sulphur hexafluoride (SF_6), hexafluoroethane (C_2F_6), and perfluoropropane (C_3F_8 or PFP). These gases are nontoxic, abundant and inexpensive, and do not require specialized hardware for hyperpolarization prior to their use in MRI, while their very short longitudinal magnetization recovery times (T_1), enables efficient signal averaging, and the high gyromagnetic ratio of ^{19}F, promises improved SNR in the lung images.

1.2 Motivation of the study

To better understand and develop these novel lung imaging techniques, a vast number of pre-clinical small animal experiments using rats and mice have been conducted [8-11]. Due to the different experimental protocols for small animal imaging experiments, as well as their small sizes, it is always preferable and desirable to build dedicated RF coils that are optimized for each different experiment, and more importantly, to quantitatively evaluate and improve their performances that directly affect the signal and image quality, such as the generated field homogeneity and coil sensitivity. In addition, it is commonly required in many lung imaging experiments to acquire both the proton images for anatomical structure information, and non-proton images for the structural and functional information of the lungs. In order to perform an accurate image registration, the experimental subject shouldn't be moved during the two different scan protocols. This will require a coil tuned to work at both the proton frequency and the non-proton frequency, or two coils tuned to two different frequencies working in close proximity.

1.3 Scope of the thesis

In this work, two sets of RF coils were developed and optimized for rat lung imaging experiments using inert fluorinated gases and hyperpolarized xenon gas. For ^{19}F rat lung imaging experiments, a quadrature-driven birdcage coil dedicated for rat lung imaging experiments was developed. Improvement in sensitivity and power consumption obtained from the quadrature structure were measured and studied. The generated B_1 field homogeneity was quantitatively investigated, and a B_1 field map in the middle of the coil was

generated. Phantom spectroscopy and imaging scans and *in vivo* rat lung imaging scans were performed.

For hyperpolarized xenon lung imaging experiments, a double-birdcage coil working at proton and xenon frequencies was developed; the decoupling between the two coils was quantitatively measured and optimized. The Q factors of the two coils were measured and compared before and after the double-birdcage coil was constructed. ^{1}H - ^{129}Xe dual-nuclei imaging scans and image registrations were performed on phantoms.

Chapter 2 introduces the fundamental principles and physics of nuclear magnetic resonance.

Chapter 3 discusses the theories of RF coil design for NMR and MRI. The essential parameters of a RF coil are generally explained. The principal and resonance modes calculation of a birdcage coil are discussed.

Chapter 4 discusses the design and construction of the ^{19}F quadrature birdcage for rat. The tuning of the resonance frequency and impedance matching using Balun circuits are described. The sensitivity and power consumption improvement from the quadrature structure are measured and verified. A method to quantitatively measure the homogeneity is discussed and the B_1 map in the center of the coil is generated. Phantom scan results and *in vivo* rat lung imaging scan results are presented and discussed.

Chapter 5 discusses the design and construction of the ^{1}H - ^{129}Xe double-birdcage coil. The coupling issue between the two birdcage coils are discussed and the optimization of the decoupling are presented. The Q factors measurements and comparison for both two coils are discussed. Phantom scan results and the image registration result are presented and discussed.

Chapter 6 presents the conclusion that can be drawn from the thesis, as well as the areas of future work.

CHAPTER 2 NUCLEAR MAGNETIC RESONANCE

2.1 Spin Angular Momentum

Spin angular momentum, like mass and charge, is an intrinsic property of the nuclei. In quantum mechanics, this property is characterized by spin quantum number I, which is either an integer or half integer. Spin of a nucleus can be considered as a sphere of distributed charge rotating about its own axis, and the small current resulted from this rotation gives rise to a "magnetic moment". The orientation of the magnetic moment is random without the presence of an external magnetic field, and its magnitude is:

$$\mu = \gamma \hbar \sqrt{I(I+1)} \, , \tag{2-1}$$

where $\hbar = h / 2\pi$, where h is Planck's constant, and γ is gyromagnetic ratio, defined as,

$$\gamma = \frac{ge}{2m} \, , \tag{2-2}$$

where g is the Lande g-factor, e is the charge of an electron, and m is the mass of the nucleus.

When the spins are placed in a magnetic field B_0, the energy of the nuclei is splitted into 2I+1 states, known as Zeemann effect. Taking proton for example, which has the I = 1/2, the two energy states are:

$$E_{\pm 1/2} = \pm \frac{\gamma}{2} \hbar B_0 \, . \tag{2-3}$$

These two energy states correspond to the magnetic moments being aligned in parallel with B_0 and anti-parallel with B_0, respectively. A transition between these two energy states can happen by absorbing or emitting the energy equal to the energy difference between them.

$$\Delta E = \hbar \omega = \left| \gamma \hbar B_0 \right| \, . \tag{2-4}$$

Combining equation (2-3) and (2-4) equation, one obtains,

$$\omega = \gamma B_0 \, , \tag{2-5}$$

where ω is called Larmor frequency. The above equations show that a transition between the two energy states occurs only when absorbing or emitting electromagnetic energy at this frequency.

2.2 Bulk Magnetization and Polarization

When a group of spins is placed in an external magnetic field B_0, each spin aligns in either parallel or anti-parallel with the field, as described above. In real NMR process, one usually deals with a large number of spins, rather than just one. To describe their general behaviour, the concept of the net magnetization was introduced, which is the summation of all the spin magnetic momentum vectors.

At room temperature, the number of spins in the parallel state N^+ is slightly higher than that of anti-parallel state N^-. The difference in the numbers between the spins in these two states is given by Boltzman statistics:

$$\frac{N^+}{N^-} = e^{(\Delta E / kT)} = e^{(-\gamma \hbar B_0 / kT)}, \tag{2-6}$$

where k is Boltzmann constant and T is the absolute temperature. If the total number of spins N is $N^+ + N^-$, then the population difference is given as:

$$N^+ - N^- = n \frac{1 - e^{(-\gamma \hbar B_0 / kT)}}{1 + e^{(-\gamma \hbar B_0 / kT)}} = n \tanh(\gamma \hbar B_0 / 2kT). \tag{2-7}$$

The polarization P of the spins is defined as:

$$P = \frac{N^+ - N^-}{n} = \tanh(\gamma \hbar B_0 / 2kT) \approx \gamma \hbar B_0 / 2kT. \tag{2-8}$$

Therefore the magnitude of the net magnetisation vector is;

$$M = M_0 = \frac{N \gamma^2 \hbar^2 B_0 I(I+1)}{3 k_B T}. \tag{2-9}$$

2.3 Interaction with external magnetic field - Precession

This magnetization, when put into an external static magnetic field B_0, will experience a magnetic torque. The motion of the magnetization M can be described by the equation:

$$\frac{d\vec{M}}{dt} = \gamma \vec{M} \times \vec{B} .$$

(2-10)

In laboratory frame of reference, assuming a uniform external magnetic field B in the direction of z axis, $B = B_0$, the above equation can be rewritten with three coupled linear equations representing the three components,

$$\frac{dM_x}{dt} = \gamma M_y B_0 ,$$

$$\frac{dM_y}{dt} = -\gamma M_x B_0 ,$$

(2-11)

$$\frac{dM_z}{dt} = 0 .$$

Further derive the first and second equation above, giving:

$$\frac{d^2 M_x}{dt^2} = -\gamma^2 B_0 M_x ,$$

$$\frac{d^2 M_y}{dt^2} = -\gamma^2 B_0 M_y ,$$

(2-12)

Set the initial conditions as $M_x(0)$, $M_y(0)$, and $M_z(0)$, the solutions to above equations are:

$$M_x(t) = M_x(0)\cos(\gamma B_0 t) + M_y(0)\sin(\gamma B_0 t) ,$$

$$M_y(t) = -M_y(0)\sin(\gamma B_0 t) + M_x(0)\cos(\gamma B_0 t) ,$$

(2-12)

$$M_z(t) = M_z(0) .$$

Equations (2-12) describe the motion of the magnetization in an external field. They indicate that the magnetization precesses about the magnetic field B_0 at Larmor frequency, as shown in Fig 2.1 below.
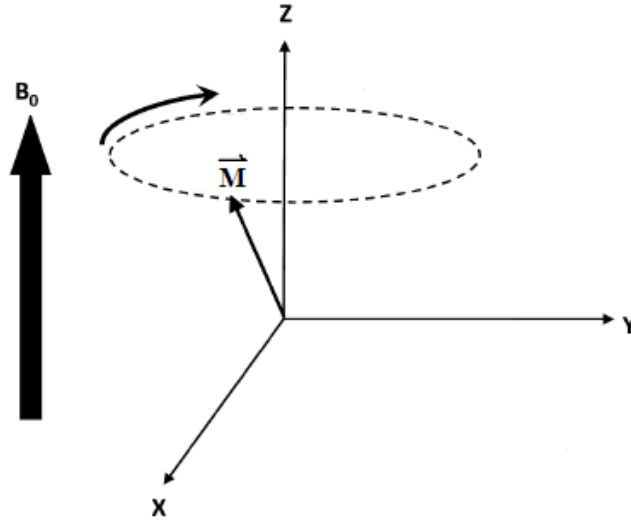
Figure 2.1 Spin precession. A Spin M, precesses around Bo at Larmor frequency.

2.4 Spin Excitation and Relaxation

When a second magnetic field B_1, generated by a RF pulse of Larmor frequency, is applied to the magnetization, by absorbing the energy from the B_1 field, the magnetization will then be "pushed" and tilted away from the z axis. This is called "excitation" of the magnetization, which is often described by the flip angle,

$$\alpha = \int_0^\tau \gamma B_1(t)dt ,$$
(2-13)

where t is the duration of the RF pulse.

Following the RF pulse, the magnetization starts to relax in two directions at the same time. In the "longitudinal" direction which is in parallel with the external magnetic field, the magnetization recovers back to its equilibrium state. This process is called "spin-lattice" relaxation, or T_1 relaxation. The rate of this relaxation is governed by the equation:

$$\frac{dM_z}{dt} = \frac{M_0 - M_z}{T_1},$$

(2-14)

where M_0 is the magnetization in equilibrium state, and M_z is the magnetization in longitudinal direction. The solution to this equation is,

$$M_z = M_0(1 - e^{-(1/T_1)}).$$

(2-15)

After a time period of T_1, the longitudinal magnetization is recovered to 63% of M_0, and after five times T_1, it is recovered back to equilibrium M_0.
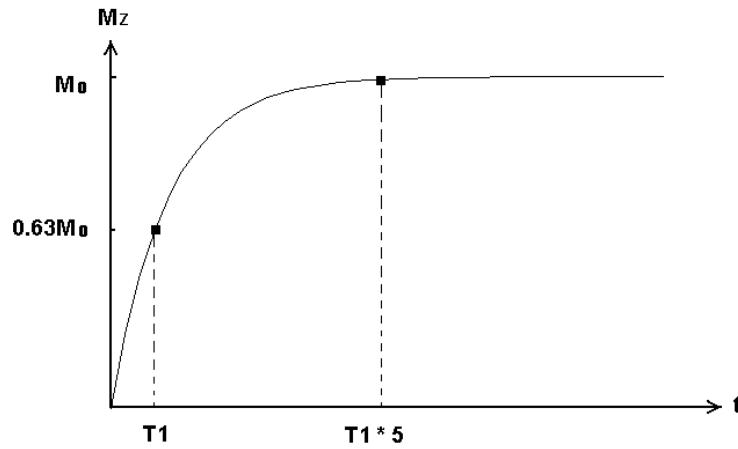
Figure 2.2 T_1 relaxation of the magnetization.

At the same time, the magnetization in the "transverse" plane, which is orthogonal to the external magnetic field, starts to lose its phase coherence because the protons are experiencing different fields due to the interactions with adjacent protons. Transverse magnetization eventually relaxes back to zero. This process is called "spin-spin" relaxation, or T_2 relaxation. The rate of this relaxation is governed by the equations:

$$\frac{dM_x}{dt} = \frac{-M_x}{T_2},$$

(2-16)

$$\frac{dM_y}{dt} = \frac{-M_z}{T_2},$$

(2-17)

18

where M_x and M_y are the magnetization components in x and y directions in the transverse plane. The solutions of there equations are,

$$M_x(t) = M_x(0)e^{-(t/T_2)},$$ (2-18)

$$M_y(t) = M_y(0)e^{-(t/T_2)}.$$ (2-19)

After the time period of T_2, the transverse magnetization is recovered to 37% of $M_{xy}(0)$.
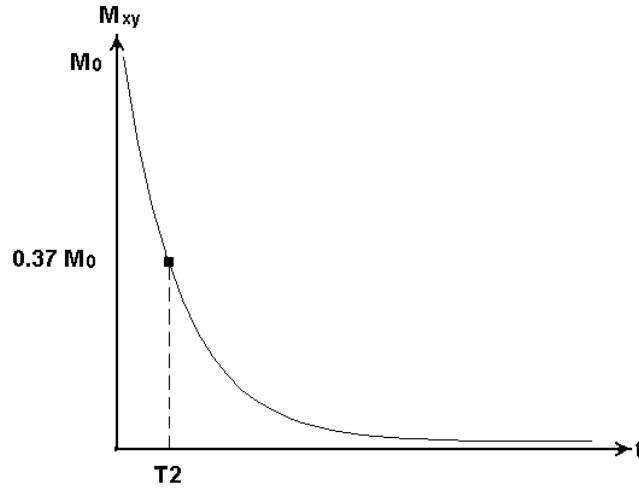
Figure 2.3 T2 relaxation of the magnetization.

2.5 Bloch Equations and FID Signal

When the previous equations of motion with the equations of relaxation are combined, the complete equations of motion for the magnetisation, known as Bloch equations, are obtained:

$$\frac{dM_x}{dt} = \gamma M_y(B_0 - \frac{\omega}{\gamma}) - \frac{M_x}{T_2},$$

$$\frac{dM_y}{dt} = \gamma M_z B_1 - \gamma M_x(B_0 - \frac{\omega}{\gamma}) - \frac{M_y}{T_2},$$ (2-20)

$$\frac{dM_z}{dt} = \gamma M_y B_1 - \frac{(M_z - M_0)}{T_1}.$$

19

During the process of spin relaxation, an oscillating magnetic field will be generated that can be detected by a coil tuned to resonate at the same frequency. According to Faraday's Law of Induction, the magnetic flux through the coil loop will then induce an electromagnetic force across the coil, kwon as the Free Induction Decay (FID) signal. The FID signal decays exponentially immediately after the magnetization starts to relax. By applying gradient magnetic fields and spacially encoding the FID, various MR images can be obtained.

2.6 Magnetic Resonance Imaging (MRI)

2.6.1 Slice selection

MRI is a tomography technique, which means it generates a cross-sectional image of the human body in a certain direction. Hence the first step of generating a MRI image is to determine the slice to be imaged and distinct it from the rest of the body (or a sample). This is achieved by adding a gradient magnetic field to the existing main magnetic field B_0 to make it increasing (or decreasing) gradually within a certain range that enclose the slice of interest. From previous sections, we know that Larmor frequency is proportional to the magnetic field strength, thus by applying a RF pulse at a frequency of the Larmor frequency of a particular slice, the spins within this slice can be excited only, whilst the rest will remain unaffected.
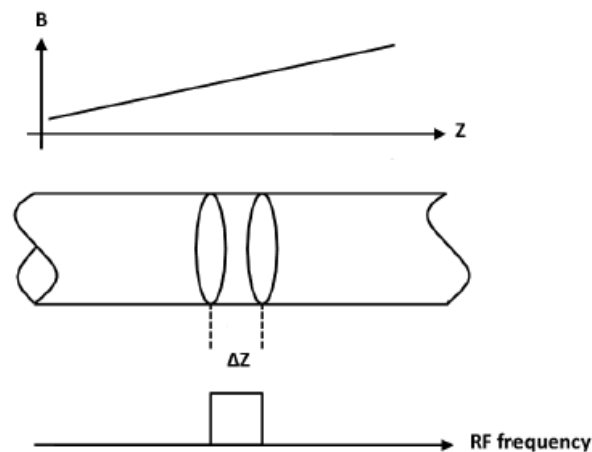
Figure 2.4 Slice selection. Z is the direction of main magnetic field. A slice of thickness Δz is selectively excited by the RF pulse of the corresponding frequency.

2.6.2 Spatial encoding

Once the slice has been selectively excited, one has to identify the spatial position of an MR signal. This is achieved by spatial encoding, which consists of phase encoding and frequency encoding of the MR signals in two orthogonal directions (here defined as x and y directions).

For phase encoding, after the spins have been excited, a magnetic field gradient in the y-direction is switched on for a short amount of time. This phase-encoding gradient changes the Larmor frequencies of the spins according to their location along the gradient. As a result, after the gradient is switched off, all spins return to their initial Larmor frequency, but a phase shift has been developed among the spins, meaning that phase varies linearly along the y-axis and each line within the slice can thus be identified by its unique phase, as shown in Fig.2.5 (a).

The second spatial encoding of the MR signal is realized by changing the frequencies along the x direction. Similar to the phase encoding, a frequency-encoding gradient is applied in the x direction. This gradient changes the Larmor frequencies of the spins along the x direction. When one is sampling the MR signal while the frequency-encoding gradient is switched on, not single frequency but a whole frequency spectrum is obtained. Now each column of the slice is identified by a specific frequency, as shown in Fig.2.5 (b).

Phase and frequency together enable spatial identification of each element, defined as "voxel".

(a)   (b)
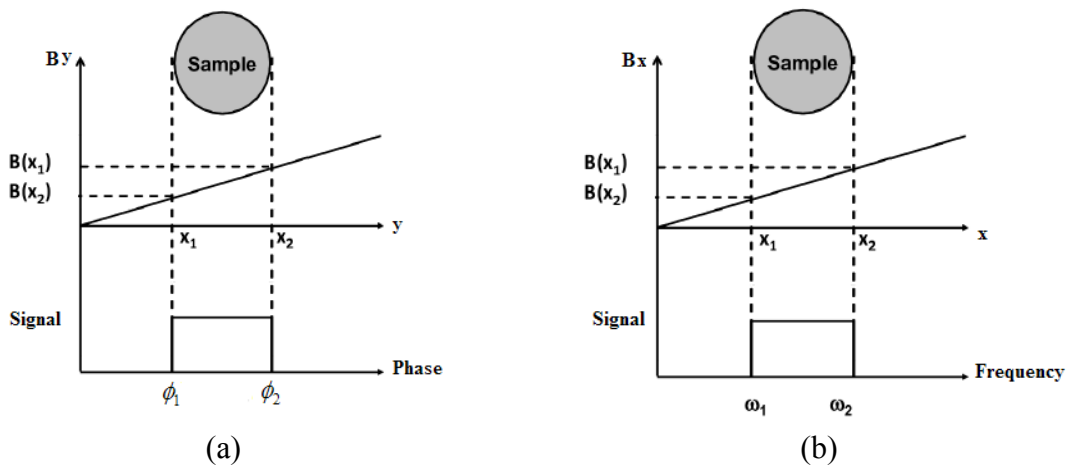
Figure 2.5 (a) Phase encoding in y direction, and (b) frequency encoding in x direction.

2.6.3 K-space and image reconstruction

When a MR signal is sampled after being spatially encoded as described above, it contains two information contents, frequency and phase. The frequency locates the signal along the x-axis and it can be extracted directly by applying a Fourier transform to decompose the signal into its frequency components along the frequency encoding direction (x direction in this case). On the other hand, the phase distribution within each frequency provides information of the position of the corresponding signal component along the y direction. However, the phases of the individual spins cannot be derived from a single signal but can only be extracted from a set of signals, thus in an imaging scans, the excitations are usually repeated with a different phase encoding gradient strength each time, to provide a sets of MR signal in order to derive the phase encoded spatial information via a second Fourier transform. To do so, each spatially encoded MR signal will then be recorded in a mathematical space, called k-space. It is a matrix of sampled MR signals, and by applying a 2D Fourier transform on the k-space data, and NMR image can be reconstructed.

2.7 Hyperpolarized Noble Gases MRI

Hyperpolarisation is a technique that increases the polarisation of a nucleus to be five orders of magnitude (about 100,000 times) higher than its equilibrium polarisation. This drastic increment in polarisation will increase the signal from the nucleus by a proportionate amount. This overcomes the signal loss from the lower gas density, which is about 3 orders of magnitude lower than that of protons. Noble gases, specifically ^{3}He and ^{129}Xe, are most widely used contrasts for hyperpolarisation MRI. This is mainly because of their nuclei possessing long spin-lattice relaxation times (T_1), and also 3He and 129Xe are the only non-radioactive noble gases with a spin number of 1/2.

Spin exchange optical pumping (SEOP), is a well-established method for noble gases hyperpolarisation. In this method, angular momentum is transferred indirectly from a polarised laser beam to 129Xe or 3He nuclei via alkali metal atoms (usually rubidium). For 3He, metastable exchange optical pumping (MEOP) is an alternative method to SEOP. In this method, hyperpolarization is created directly in the nuclei via polarized laser, when 3He atoms are excited to the metastable state by a radiofrequency discharge.

In conventional MRI, after a RF pulse has excited the longitudinal magnetisation (Mz), it recovers to thermal equilibrium by T_1 relaxation. For hyperpolarized gases, the longitudinal magnetisation will not recover, and each RF pulse destroys a portion of the longitudinal magnetisation. For such a reason, one normally uses a small flip angle in each excitation to achieve a full k-space sampling. Since there is no longitudinal recovery, the repetition time, TR, can be made as short as possible to reduce the scan time, and the signal detected from the nth excitation is given by [13]:

$$S(n) \propto M_Z(0)e^{[-(n-1)(\frac{T_R}{T_1})]} \cos^{(n-1)} \alpha \sin \alpha . \qquad (2\text{-}21)$$

And the longitudinal polarization remained available for the nth excitation is:

$$M_Z(n) = M_Z(0)\cos^{(n-1)} \alpha . \qquad (2\text{-}22)$$

CHAPTER 3 RF COILS THEORY

3.1 Transmission and Reception

In NMR processes, RF coils are used for two purposes: during transmission, they generate a magnetic field (B_1 field) to excite the magnetization, and during reception, they work as receivers to detect the FID signal from the spin relaxation process. The principle of a transmit coil is governed by one of the most primary laws in electromagnetism, Ampere's law:

$$\frac{1}{\mu_0} \oint B \cdot dl = \int_S J \cdot dS .$$

(3-1)

After the excitation, a rotating magnetic field resulted from the precession of the magnetization will generate an induced EMF in the receive coil according to the Faraday's law of induction,

$$\xi = \oint E \cdot dl = -\frac{d}{dt} \int_S B \cdot dS .$$

(3-2)

As a transmit coil, it is usually expected to be able to generate a most uniform rotating magnetic field B_1 over a region of interest in a subject. On the other hand, as a receive coil it is essential to have a high signal sensitivity to ensure a maximized SNR. Though it has been experimentally verified that there is reciprocity nature between the RF signals in transmitting and receiving process [12], due to the different preferences of coil performances in transmitting and receiving modes, it is very common to use separate coils for transmitting and receiving, as each coil can be designed and optimized for different performances. For example, volume coils are usually used as a transmitting coil due to their symmetrical structure and thus the intrinsic advantage in field homogeneity, while a surface is more preferred for signal receiving because of its high sensitivity. Nevertheless, a single coil with optimized design can be used for both.

3.2 Resonance Circuits and Coil Tuning

RF coils are generally designed to be resonant at the Larmor frequency of at least one certain nucleus of interest under a given external magnetic field strength. A coil can always be described using a lumped element RLC equivalent circuit [14]. The probe of a coil is made of an inductor of inductance L with resistance of r, and by adding capacitive component C it can be tuned to a desired frequency.
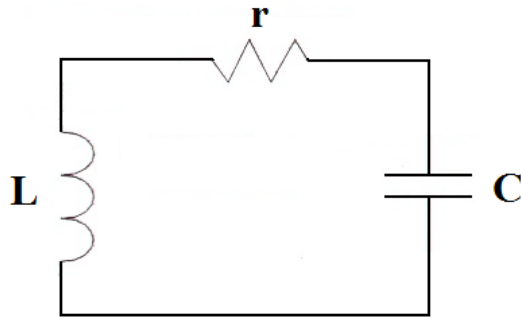
Figure 3.1 Equivalent RLC resonant circuit of a coil.

The total impedance of this equivalent circuit can be expressed as a complex number:

$$Z = R + jX_\omega,$$

(3-3)

where X_ω is the total reactance of the probe inductor and capacitors, and equals to $X_L + X_C$, where,

$$X_L = \omega L,$$

(3-4)

$$X_C = \frac{1}{\omega C}.$$

(3-5)

The resonant circuit comes to resonance at frequency ω when X_ω is minimized to zero, giving the resonance condition,

$$\omega = \frac{1}{\sqrt{LC}}.$$

(3-6)

When this resonant condition for a coil is met, the electric and magnetic energy transfer equally between reactive components at the resonant frequency during each cycle, and only dissipates energy through the real resistance R, governed by Ohm's law,

$$W = \frac{1}{2} I^2 R ,$$

(3-7)

where I is the current in the coil.

The impedance of a coil at its input / output port then can be expressed as:

$$Z = \frac{(r + j\omega L) \dfrac{1}{j\omega C}}{r + j\omega L + \dfrac{1}{j\omega C}} .$$

(3-8)

3.3 Q Factor

In a resonant coil, energy is oscillating electrically and magnetically between the reactive components. The efficiency of the coil can be measured by quality factor Q, which is defined as the ratio of the energy stored in the coil to the energy dissipated during one cycle,

$$Q = 2\pi \cdot \frac{Energy_{Stored}}{Energy_{Dissipated}}$$

(3-9)

The Q factor of a coil of inductance L and resistance r is given as

$$Q = \frac{\omega L}{r}$$

(3-10)

Another way of defining the Q factor is given in term of the frequency bandwidth as,

$$Q = \frac{f_0}{\Delta f} \qquad (3\text{-}11)$$

where f_0 is the resonant frequency and Δf is the bandwidth, defined as the frequency range between two frequencies of the half peak power value. A typical value of Q for a NMR coil is between 50 and 500 [14], depending on the loading conditions.

3.4 Impedance Matching

Transmitting the signal from the coil to the pre-amplifier efficiently is as important as detecting a strong FID signal from the coil. Matching the probe impedance to that of the transmission line, which is usually 50 Ω, is crucial to avoid any re-flections which leads to higher power consumption and image signal loss. The reflection coefficient can be expressed as the ratio of voltage of the reflected signal V⁻ and that of the input signal V⁺:

$$\Gamma = \frac{V^-}{V^+} . \qquad (3\text{-}12)$$

Also, it can be written as:

$$\Gamma = \frac{Z_{Coil} - Z_{TL}}{Z_{Coil} + Z_{TL}} , \qquad (3\text{-}13)$$

where Z_{coil} and Z_{TL} are the coil and transmission line impedance, respectively. In order to assure maximum power dissipation in the load and minimize the reflection, the impedance of the load should be maintained the same as that of the transmission line (normally 50 Ω). This can be achieved by transforming the impedance of the load using conjugate matching method, in which the imaginary part of the load impedance is cancelled via an impedance matching circuit, whose impedance Z_M is a conjugate value of that of the load:

$$Z_M = Z_{Coil}^* . \qquad (3\text{-}14)$$

The real part of the impedance is then equal to, or can be transformed to that of the transmission line, via an impedance transforming circuit (such as a Balun), and thus minimize the reflection coefficient to be zero.

3.5 Signal to Noise Ratio (SNR) and Signal losses

3.5.1 SNR

As described in Chapter 2, NMR signal is generated by the precession of nuclear magnetization in the B_0 field. The magnetization can be given by:

$$M_0 = \frac{\chi B_0}{\mu_0} = \frac{N\gamma^2\hbar^2 I(I+1)B_0}{3k_B T_S} \,, \qquad (3\text{-}15)$$

where χ is the susceptibility of the sample, N is the number of spins, γ is the gyromagnetic ratio, I is the spin quantum number, k_B is Boltzmann's constant, T_S is the sample temperature.

The magnetization, when excited by a circularly polarized magnetic field B_1 generated by a coil, will precess at an angle of Φ in B_0 at frequency ω, and induces a voltage in the receive coil according to Faraday's law of induction. The voltage signal can be expressed as:

$$S = M_0 \int_S \omega \sin\varphi B_1(r)\mathbf{d}V \,. \qquad (3\text{-}16)$$

From equation (3-15) and (3-16), the signal received can be expressed as:

$$S = (\frac{n_s\gamma^2\hbar^2 I(I+1)B_0 B_1}{3k_B T_S})\sin\varphi V \,. \qquad (3\text{-}17)$$

Johnson-Nyquist noise (or thermal noise) is the dominant noise in NMR, which arises from random electrical fluctuations created by Brownian motion of electrons. The mean square voltage induced by the thermal noise in a conductor of resistance R, temperature T and bandwidth Δf is:

$$N = \sqrt{4Rk_B T\Delta f} \,. \qquad (3\text{-}18)$$

Coil and sample are both the main sources of thermal noise in NMR. In reality, a coil is made of an inductor with a resistance (Rc), and the sample, when coupled to the coil, will be seen as a equivalent resistor (Rs). Other noises such as background radiation and interferences

usually are or can be made negligibly small. Considering $R = R_c + R_s$, the total noise signal generated in a loaded coil can be expressed as:

$$N = \sqrt{4(R_C + R_S)k_B T \Delta f} \; . \tag{3-19}$$

From equation (3-17) and (3-19), the SNR can be calculated as:

$$SNR = \frac{V_{Signal}}{V_{Noise}} = \frac{n_s \gamma^2 \hbar^2 I(I+1)B_0 \sin \varphi B_1 V}{8 k_B^{3/2} T^{3/2} \sqrt{(R_C + R_S)\Delta f}} \; . \tag{3-20}$$

3.5.2 Coil loss and sample loss

In equation 3-20, R_C and R_S represent coil loss and sample loss, respectively. In order to get an improved SNR, both the two losses should be minimized.

Coil loss is caused by both the power dissipated to the Ohmic resistances of the copper wire and the electrical components, and radiation loss. Power dissipated in the equivalent resistor that is introduced by non-ideal components, such as inductors and capacitors, will transfers into heat and causes loss in signal. On the other hand, an ideal RF coil would be expected to act more as an energy conserving coil and less as a radiating antenna. However, in reality coils inevitably lose energy to the surrounding free space due to radiation. To minimize the radiation loss, one should generally limit the size of the coil under 0.1λ, where λ is the wavelength of signal. Besides, using distributed capacitors to break the coil inductor into multiple shorter sections will also reduce the radiation loss.

Sample loss is another major cause that degrades the SNR. During transmission of the B1 field, eddy currents will be induced in the sample, which is within the field. Some of this transmitted power is dissipated within the sample and causes local sample heating. Based on the principle of reciprocity of the RF coil, these eddy currents will then induce voltages in the receiver coil causing noise. On the other hand, because of the dielectric effect of the sample, displacement currents will also be introduced to the sample, which causes dissipation within the sample, and through the capacitive coupling between the sample and the coil, generates noise in the receiver coil.

3.6 Filling Factor

A magnetic filling factor η_f is defined as [15]:

$$\eta_f = \frac{\int B_1^2 dV}{\mu_0 U},$$

(3-21)

where U is the total energy in the magnetic field, and the integration of a constant field B_1 is over the sample volume. This is the ratio of the energy in the positive rotating circularly polarized field, to the total magnetic energy. The above equation can lead to a useful relationship:

$$\eta_f = \frac{\beta^2}{20} \frac{V_s}{V_c},$$

(3-22)

where β is a dimensionless function of coil geometry. Vs is the sample volume, and Vc is the volume of the coil.

Usually a high filling factor is desired. To maximize the filling factor, a volume coil should be designed to have an inner volume close to the volume of the sample.

3.7 Surface coil & Volume coil

3.7.1 Surface coil

A surface coil is a single coil placed directly next to the region being imaged, without wrapping the entire subject. In the reception mode of NMR or MRI, surfaces coils are more preferable for their higher sensitivity and thus better SNR performance. A surface coil in its simplest shape is a circular or square loop which can be represented as a simple LC circuit, and the lumped element circuit is one of the ways that can be used for modeling the coil, as shown in Figure 3.2.

(a)   (b)
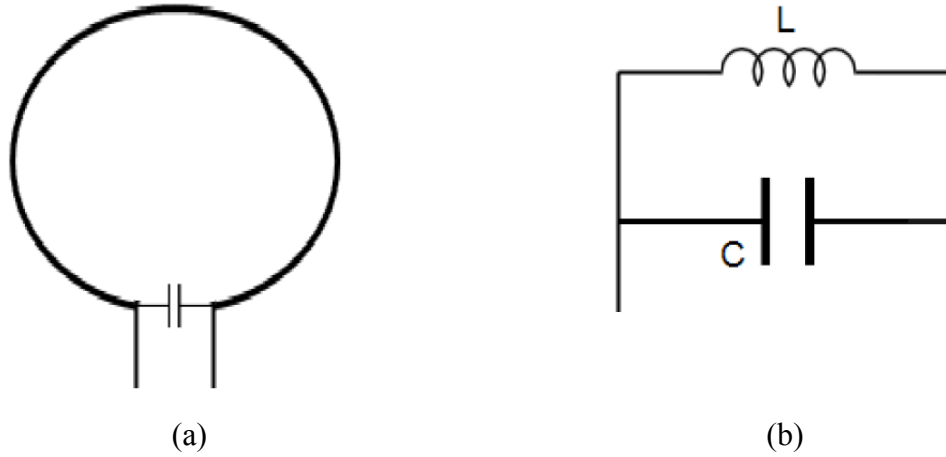
Figure 3.2 A loop surface coil (a) and its equivalent circuit (b).

In practical design, capacitors in a surface coil are usually distributed around the circumference of the coil to improve the current distribution and reduce radiation and electric losses. Despite a high SNR, surface coils are usually limited in providing a large field of view (FOV), especially in clinical imaging scans. This is because the sensitivity of a surface coil decreases along with the increment of its size. In order to overcome this problem, one can use multiple small-size surface coil elements to form a large coil array, and provide a large FOV without any cost of SNR [16], such as sensitivity-encoding (SENSE) [17].

3.7.2 Volume coil

While transmitting RF pulses, a coil is expected be able to generate a uniform magnetic field over a region of interest (ROI). A uniform rotational magnetic field can be ideally generated by a uniform current distribution on a spherical surface. Helmholtz coil is an example of this configuration. In a Helmholtz coil, two parallel loops are driven by in phase currents, and this gives a uniform field distribution. Besides, an ideally cosine current I distribution on a cylindrical surface can also generates an ideal homogeneous field within the coil, as shown in Fig 3.3. The current distribution on the surface can be expressed as:

$$I_n = I_0 \cos(\theta_n) \qquad\qquad (3\text{-}23)$$

where θ_n is the azimuthal angle and $\theta_n = 2\pi\,/\,n$, where n is a positive integer. The currents directed are along the magnet field Z direction.

The saddle coil is an approximation of this configuration with n of 4. It consists of two pairs of axial wires laid over two halves shells and connected with arc shape wires as return current loops. Saddle coils are widely used as gradient coils.
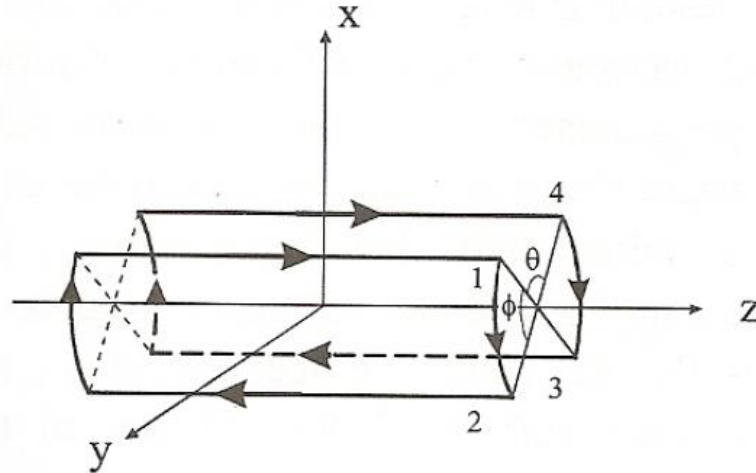
Figure 3.3 An illustrative saddle coil structure [14].

When using a receive-only surface coil in combination with a transmit-only volume coil, the two coils will couple to each other. While transmitting, a current will be induced in the surface coil and this might causes skin burns to the subject or patient. And during the reception, a portion of the FID signal will dissipate in the volume coil and deteriorate the SNR. Therefore, a decoupling circuit or PIN diodes are usually used to decouple the coils during transmission and reception.

3.8 Birdcage Coil

The concept and first design of "birdcage" coil was initially introduced by Hayes *et al.* in 1985 [18]. Birdcage coils have been widely chosen for MRI for its ability of providing circularly polarized field of high homogeneity. A birdcage coil is made of multiple parallel conductive segments (rungs) that are parallel to the external magnetic field B_0. These rungs connect a pair of conductive loop end-rings. Capacitors can be put either on the rungs, end-ring segments or both, to tune the coil to a desired frequency. A birdcage coil can be considered as a circular network of identical filter elements, each of which is connected to another and the last one is connected to the first one to form a circle. By different types of the

filter element, it can be classified as high-pass mode, low-pass mode, or band-pass mode. A typical high-pass birdcage coil and its filter element are shown in Figure 3.4 and Figure 3.5. L_1 represents the equivalent inductance in an end-ring segment, C_1 is the tuning capacitor placed in one end-ring segment, and L_2 is the equivalent inductance in a rung.
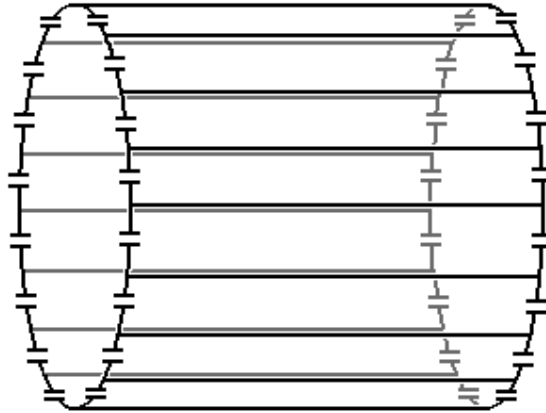
Figure 3.4 Illustrative structure of a birdcage coil in its high-pass mode.
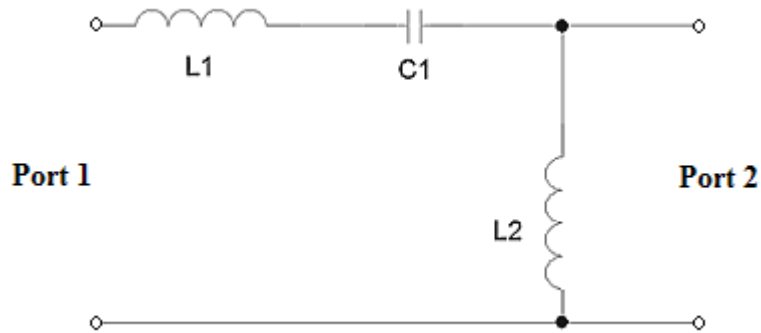
Figure 3.5 Equivalent circuit of a high–pass birdcage coil element.

There are many numerical ways to analyze the behavior of a birdcage coil. A method using ABCD matrix is very useful and effective in calculating the resonance mode of a birdcage coil [14]. Consider the filter cell as a two-port network, the total impedance of the end-ring segment consisting of the segment inductance (and the capacitance of the end-ring capacitor if a high-pass mode) is Z_1, and the total impedance of the rung consisting of its inductance (and the capacitance of the rung capacitor if in a low-pass mode) is Z_2, respectively, as

33

shown in Figure 3.6 (a). A birdcage coil of 2N rungs can be then described as a circular ladder network made of 2N elementary networks, shown in Figure 3.6 (b).

(a)   (b)
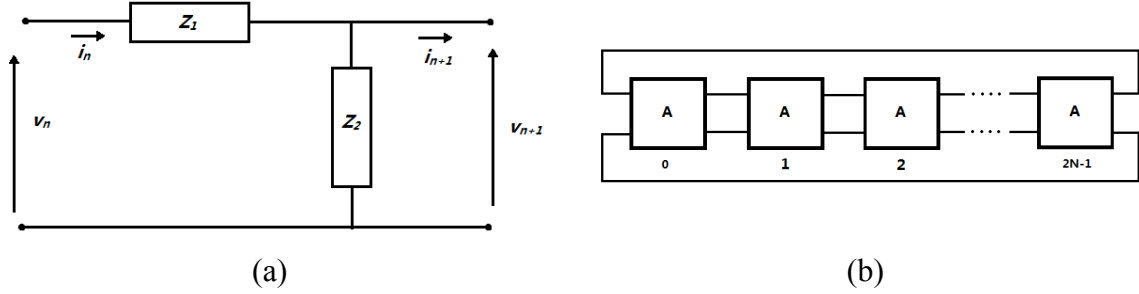
Figure 3.6 Illustrative schematic of a high-pass birdcage coil element (a), and matrix diagram of a high-pass birdcage coil (b).

Let A be the ABCD matrix of a filter element, described as,

$$
A = \begin{bmatrix} 1 + \dfrac{Z_1}{Z_2} & Z_1 \\ \dfrac{1}{Z_2} & 1 \end{bmatrix}.
$$

(3-24)

The input and output of this filter element are defined as,

$$
\begin{pmatrix} v_n \\ i_n \end{pmatrix} = A \begin{pmatrix} v_{n+1} \\ i_{n+1} \end{pmatrix}.
$$

(3-25)

For a birdcage of 2N identical elements, we have,

$$
\begin{pmatrix} v_0 \\ i_0 \end{pmatrix} = A^{2N} \begin{pmatrix} v_{2N-1} \\ i_{2N-1} \end{pmatrix}.
$$

(3-26)

Given the fact that the last filter element is connected to the first one, the input (v_0, i_0) equals to the output (v_{2N-1}, i_{2N-1}), therefore,

$$
A^{2N} = I.
$$

(3-27)

By solving equations (3-24) and (3-27), we obtained the relationship of birdcage coil resonance modes and the impedances of the end-ring segment and the rung,

$$\frac{Z_1}{Z_2} = -4\sin^2\left(\frac{k\pi}{2N}\right),$$

(3-28)

where k is an integer between 0 and N. Equation (3-28) implies that there are k resonant modes in a birdcage coil for the given end-ring segment and rung impedances [19], which are determined by the coil geometry and tuning capacitors. The currents that generate the magnetic field are distributed in the legs as:

$$I_n = I_0 \cos(\pi k n / N + \phi),$$

(3-29)

where ϕ is the spatial phase factor dependant on the way the coil is excited and usually considered 0. From the NMR point of view, the $k = 1$ mode is usually preferred since in this mode the currents phase changes at the lowest speed in the rungs and formed a "fine" cosine distribution, thus generates a homogeneous magnetic field in the middle of the coil for excitation, as shown in the Figure 3.7 and Figure3.8.
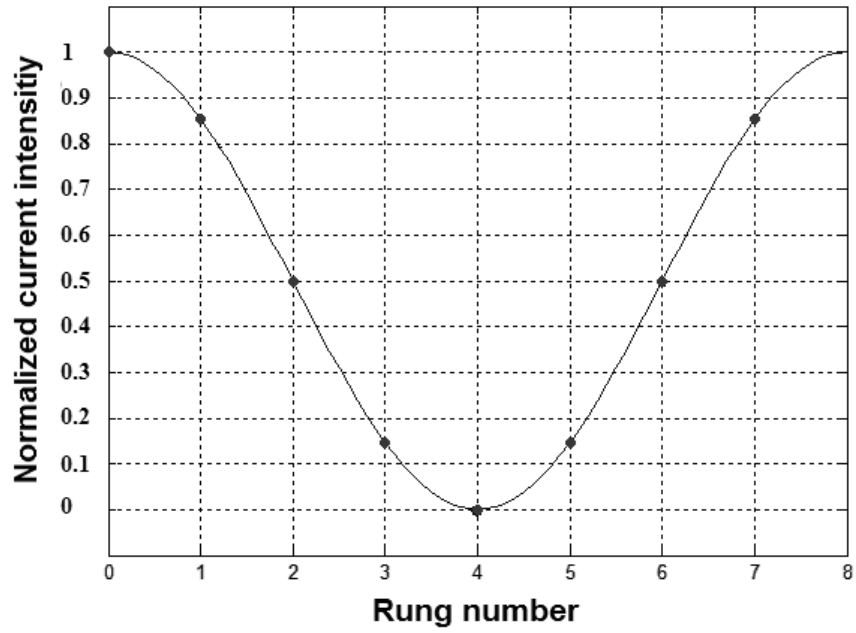
Figure 3.7 Illustrative cosine currents distribution in a 8-rungs birdcage
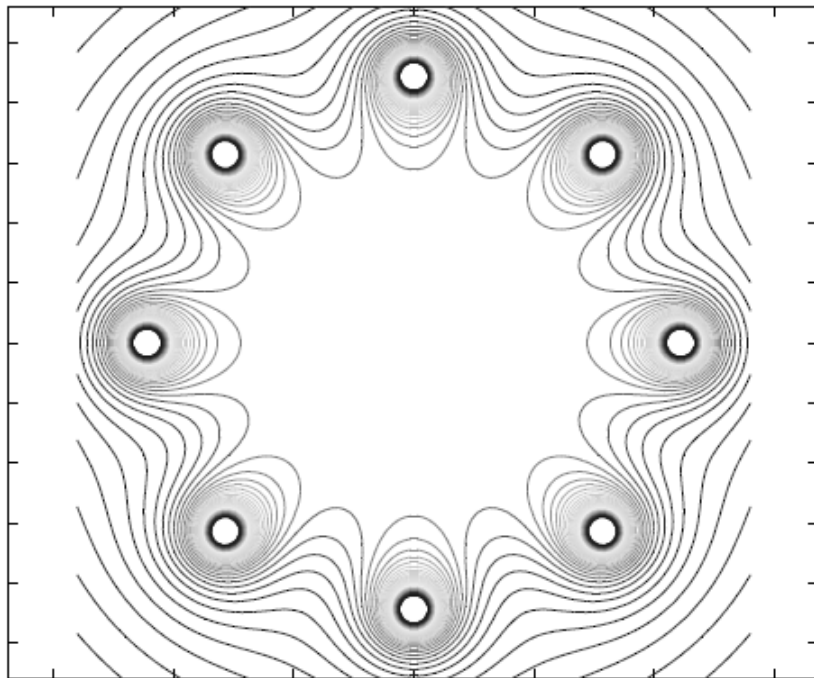
Figure 3.8 Illustrative field distribution in the transverse plane inside the birdcage coil [14].

CHAPTER 4 ^{19}F QUADRATURE BIRDCAGE COIL

4.1 Introduction

Recently, ^{19}F MRI using inert fluorinated gases such as sulphur hexafluoride (SF_6), hexafluoroethane (C_2F_6), and perfluoropropane (C_3F_8 or PFP) has shown great potential to become a useful and efficient lung imaging technique [6, 21 - 23]. Due to the high gyromagnetic ratio of ^{19}F nuclei, one can obtain sufficiently high signal intensity without the need of hyperpolarization, and the short longitudinal relaxation time (T_1) of fluorinated gases allows rapid signal averaging. Thus, these non-toxic and abundant gases have become a promising alternative to hyperpolarized noble gases as novel lung imaging contrast, and numerous ^{19}F MRI experiments using small animals have been conducted [8 - 11].

In this chapter, a quadrature-driven birdcage T / R coil dedicated for rat lung imaging experiments using inert fluorinated gases was presented. Coil construction, parameter calculations and performance tests are discussed in details.

4.2 Coil Geometry and Tuning

An 8-rungs birdcage coil was built using copper tapes sticking to the surface of a machined acrylic tube. Dimensions of the coil were carefully designed for an optimized filling factor and suitability for small animal lung imaging experiments, especially for the rats. The diameter of the tube is 90mm and the overall length is 100mm. The end-ring width and the rungs width are both 6.5mm, and the rungs length is 68.5mm. The extra space on the surface of the acrylic tube was reserved for matching circuit deployment. 8 gaps were made on each end-ring to accommodate all 16 capacitors, forming a high-pass structure.

Table 4.1 ^{19}F birdcage coil dimensions and materials

	Material	Length (mm)	Width (mm)	Thickness (mm)	Diameter (mm)
Coil frame	Acrylic tube	100	-	3.25	83.5
End-rings	Copper tape	-	6.5	0.06	90
Rungs	Copper tape	68.5	6.5	0.06	-
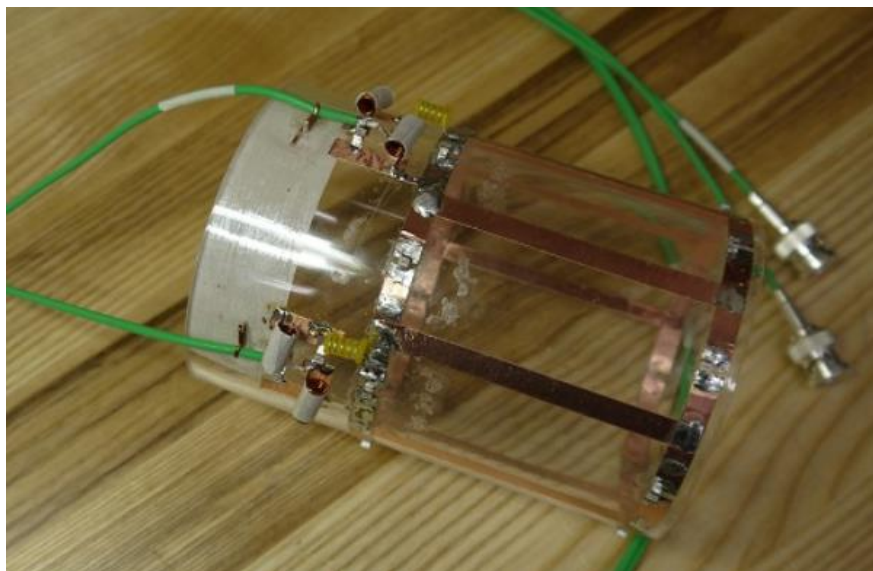
Figure 4.1 Top view of the ^{19}F birdcage coil

In order to tune the birdcage coil to 120.15MHz (the Lamour frequency of ^{19}F under 3 Tesla field), calculations for the end-ring tuning capacitor values were performed using the BirdcageBuilder software [19, 20]. With the dimensions specified above, the value of each end-ring capacitor is calculated to be 43pf. After 16 tuning capacitors were placed on the end-rings, the resonant frequency of the birdcage coil was measured using two RF pick-up probes previously tuned to 120MHz on a HP 8751A network analyzer. Specifically, the two pick-up probes were connected to the two ports of the network analyzer, and the two probe heads were placed across the birdcage coil, the resonance frequency was measured by viewing the S21 responses. The network analyzer was set at a center frequency of 120.15MHz with 10MHz span, in order to include only the dominant resonance mode of the birdcage coil.

4.3 Impedance Matching

As discussed in section 3.4, to minimize the power reflection, the impedance of a coil at its input / output port should be matched to that of the device it electrically connected, such as the network analyzer, the scanner, a transmission line, or a hybrid coupler. There're many different ways to transform the input impedance of a coil to a desired value. In this work, two L-C Balun circuits were used to match both the two ports of the coil to 50ohm impedance.

Balun (balance-to-unbalance) is a type of coupler that connects a symmetrical (balanced) circuit to an asymmetrical (unbalanced) circuit, and it provides a 180 degree phase shift between the input and output signals. L-C Balun is a type of Balun that has four components and a very symmetrical structure, as shown in Fig 4.2.
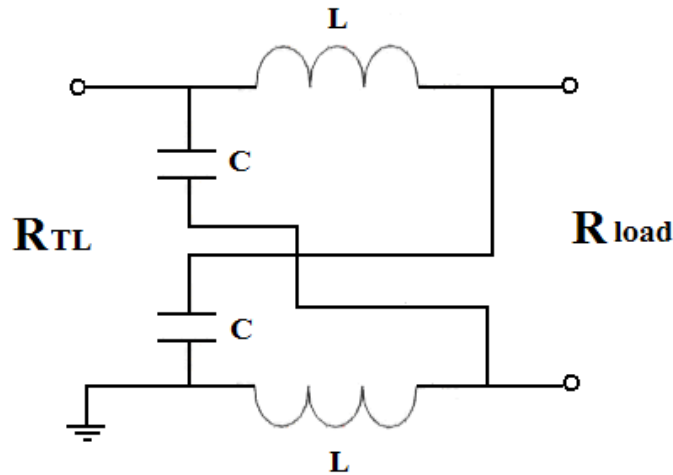
Figure 4.2 Schematics of a L-C Balun.

L-C Balun can be used as impedance transformers. In Fig 4.2, R_{TL} is the impedance of a transmission line (pure resistive), and R_{load} is the impedance of a balanced load (pure resistive). At a certain working frequency ω, define $Z_0 = \sqrt{R_{TL} R_{load}}$, then the components L and C can be calculated as :

$$L = \frac{Z_0}{\omega} \text{ ,} \tag{4-1}$$

$$C = \frac{1}{Z_0 \omega} \text{ .} \tag{4-2}$$

The impedance of a load (such as a coil) is usually a complex with a reactance component, thus when using L-C Balun as impedance transformer, one must first cancel out this reactance and leave it pure resistive. This can be done easily by adding an inductor (or capacitor) in series with the load.

As shown in Figure 4.3, L_1 and C_1 were calculated according to equations 4-1 and 4-2, with the given [19]F Larmor frequency. At 120.15MHz, L_1 is calculated to be 198nH and C is

39

calculated to be 8.9pf. Inductors L_2 were used to cancel out the imaginary part of the impedance, thus achieve a pure resistive impedance. The value of L_2 is calculated to be 35nH. The Balun matching circuits were built on the outside of the coil cylinder right next to each port.
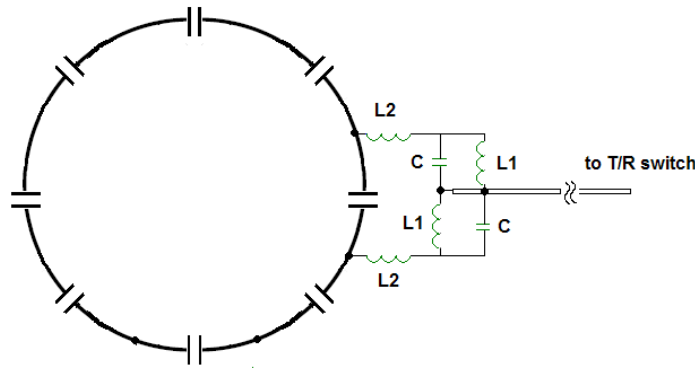
Figure 4.3 Schematics of the linear ^{19}F coil with balun impedance matching circuits.

The measurement for the impedance was performed on each port to verify and investigate the performance of the impedance matching circuits. The S11 parameters for the two ports are shown in Figure 4.3. Each port has obtained approximate 50ohm impedance.

(a)   (b)
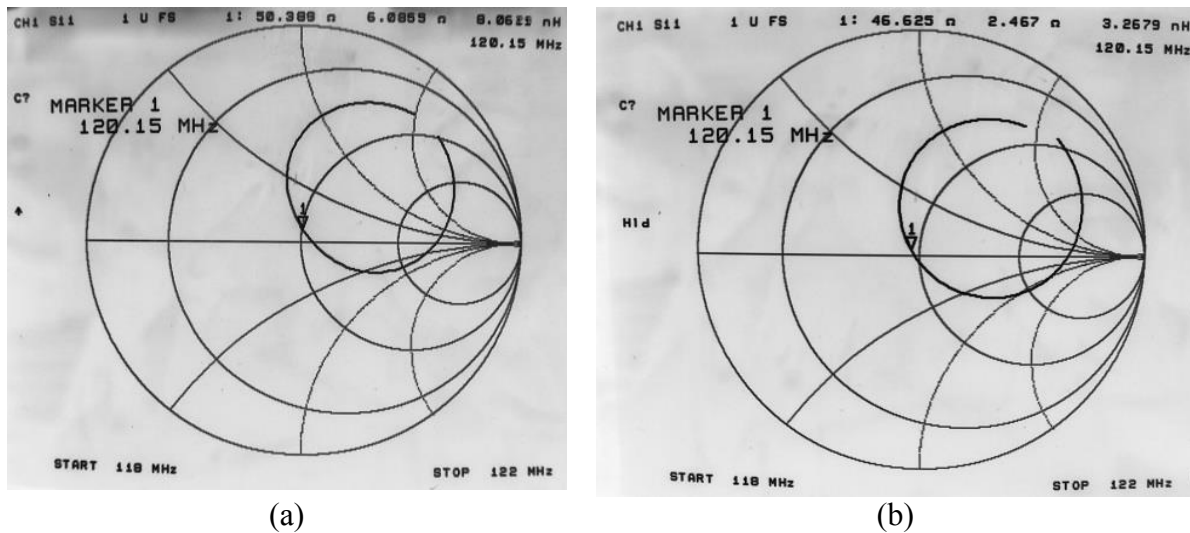
Figure 4.3 S11 responses of the two channels on Smith chart.

When coupling the birdcage coil to other equipment such as the scanner or a network analyser, one should minimize the dissymmetry introduced to the structure of the coil, to maintain an accurate tuning and a uniform B_1 field. Inductively coupling method by putting

a second loop close to the birdcage coil is one that is commonly used to keep the symmetrical structure. However, it may create some distortion of the B_1 field distribution, hence capacitive coupling methods using lumped capacitors are also commonly used. When external connections are added to the birdcage, it breaks the symmetrical structure of the birdcage coil, and thus the ideal cosine current distribution among the legs, but it can be approached very closely [14].The B1 field homogeneity of the birdcage coil presented in this work will be further studied and quantitatively mapped in Section 4.5.

4.4 Quadrature Driving

4.4.1 Quadrature mode

A RF coil can work on linear or quadrature mode, depending on the geometry and driving method. When the RF pulse is fed via a single port, the RF coil is then working at a linear mode and the generated B_1 field is linearly polarized, meaning it will be directed toward a single direction. By decomposing this linear polarized field to two components, B_1^+ that rotates clockwise, and $B1^-$ that rotates counter clockwise, we can clearly see that only one of the two components will interact with the spins during the excitation, since it rotates in the same direction with the spins, while the other component, which rotates reversely, doesn't contribute at all. On the other hand, a coil can also be fed with two signals that have a 90-degree phase shift. In this case, a circularly polarized magnetic field will be developed, meaning it will rotate in a certain direction. Hence during the excitation, when the field rotates in the same direction with the spin precession, it becomes totally efficient in exciting the spins. Therefore, compared to a linearly polarized field generated by a linearly driven coil, a quadrature-driven coil will halve the power requirement for the excitation. The linear and quadrature fields are shown in Figure 4.4.
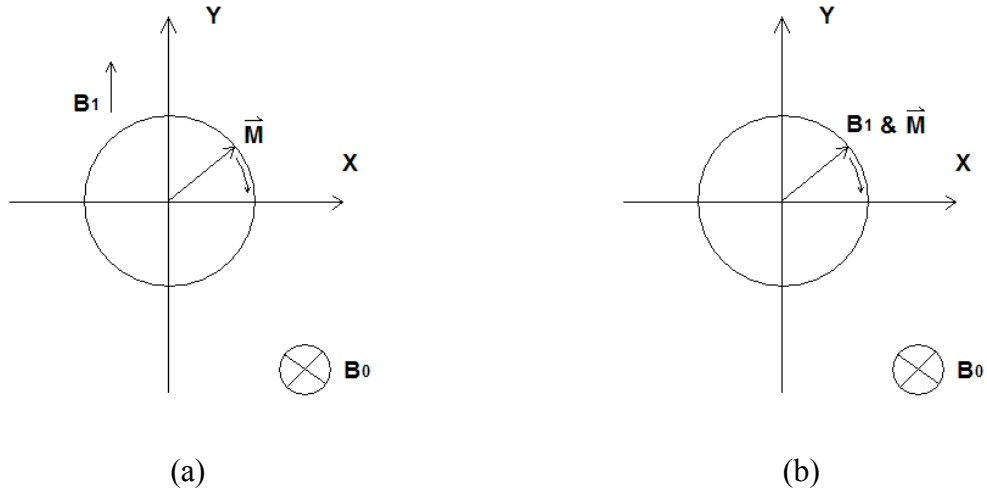
Figure 4.4 Developed B_1 magnetic field pointing toward one direction in linear mode (a), and rotating in the same direction with the magnetization in quadrature mode (b).

On the other hand, during the signal receiving, the two outputs of a quadrature coil will be combined and thus increase the signal intensity by a factor of two, while the combined noise components from the two orthogonal channels will only increase by a factor of square root two, since they are not correlated. Hence, an improvement in SNR by a factor of square root two can be gained from the quadrature-driven mode [25].

4.4.2 Quadrature coil construction

As described above, in order to implement the quadrature driving method, two signals of the same amplitude are required to be fed into two coils that are geometrically orthogonal. When these two signals have a 90 degree phase difference (electrically orthogonal), a circularly polarized field will be developed inside the coil. The quadrature mode is relatively difficult to be developed in two surface coils, since the orthogonal geometry could raise coupling issue between the two coils. In contrast, one of the advantages of the birdcage coil is that it is intrinsically suitable for working in a quadrature mode for its cylindrically symmetric structure. The original coil was re-constructed for quad-operation. Another signal feed port was added on the end-ring two segments away from the previous port. This makes the two ports geometrically perpendicular to each other in the axial plane. The impedance was matched to 50 ohm at the new port, using an identical Balun circuit.
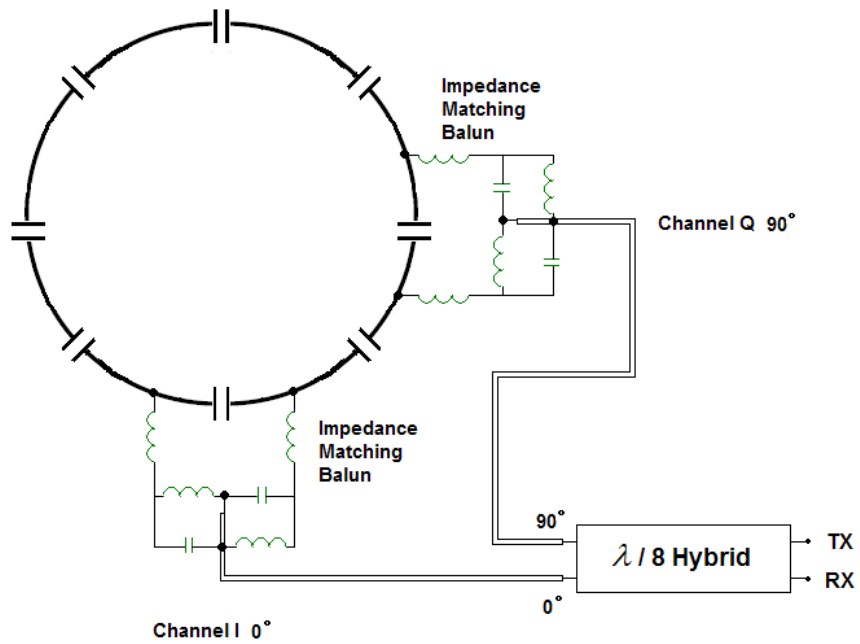
Figure 4.5 Schematics of the quadrature-driven birdcage coil with impedance matching Balun circuits for both I and Q channels.

4.4.3 λ / 8 Hybrid coupler

Hybrid coupler is a particular kind of directional couplers that divides the input power equally for two outputs. There are many ways to implement a hybrid coupler for microwave frequencies [26]. As described before, in order to implement a quadrature driving method, one needs to create two Tx signals of the same amplitude having a 90-degree phase shift. A λ / 8 hybrid coupler was used in its lumped elements equivalent circuit for such an implementation, to maintain a desirable device dimensions. Figure 4.6 shows the structure of a λ / 8 hybrid built with two transmission lines of the standard characteristic impedance, where $C = 1 / Z_0 \, \omega$.
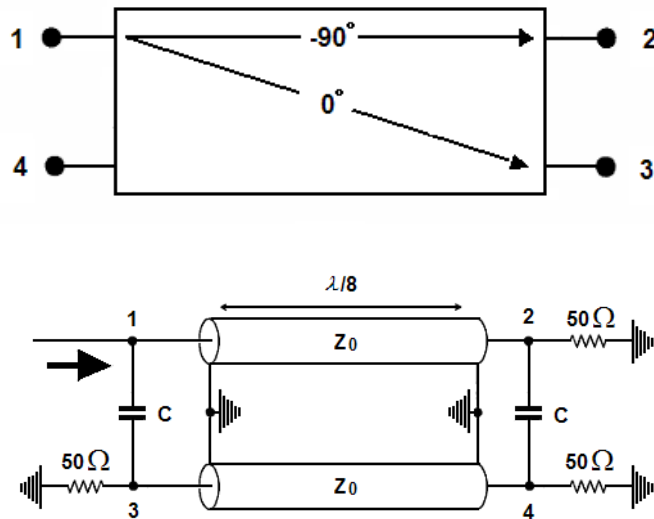
Figure 4.6 Signal phase shifting (a) in a λ / 8 hybrid coupler (b).

As previously mentioned, the Larmor frequency of ^{19}F at 3T magnetic field is 120.15MHz, which corresponds to a λ / 8 of 31.21cm. To make the hybrid circuit in a minimum size, the two original transmission lines were replaced using lumped elements equivalent circuits.
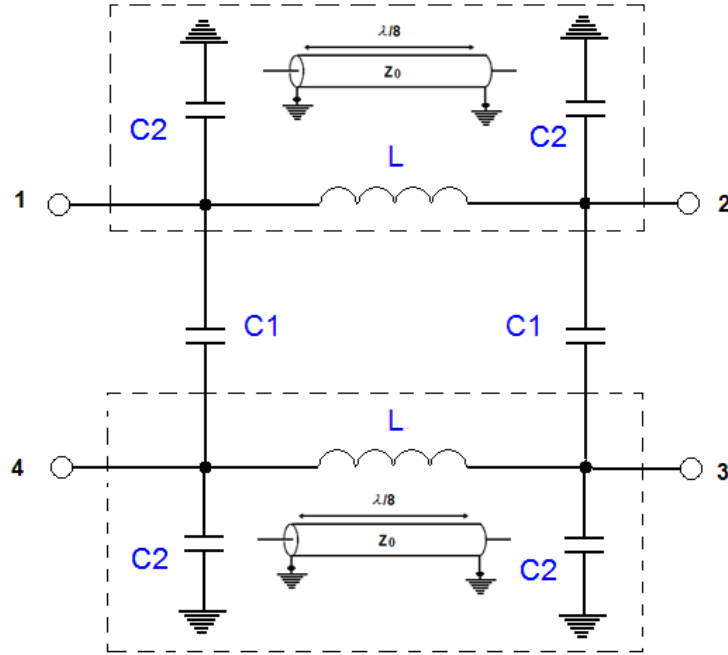
Figure 4.7 Equivalent circuit of a λ / 8 hybrid coupler.

As shown in the Figure 4.7, the λ / 8 transmissions lines are replaced by the Pi-network equivalent circuit, illustrated in the dash-line box. Obviously C_1 equals to C in Figure 4.6, and is $1 / Z_0 \omega$. To calculate the values of C_2 and L, which are components in a Pi-network, the equations below are used, given that all the ports are matched to 50ohm,

$$X_c = \frac{Z_0}{K},\tag{4-1}$$

$$X_L = Z_0 \frac{2K}{K^2 + 1}.\tag{4-2}$$

The value of *K* can be determined by a condition derived from the character of the transmission line, that is, a λ / 8 transmission line of characteristic impedance of Z_0 will exhibit an impedance of jZ_0 when shorted. Hence,

$$\frac{1}{jZ_0} = \frac{1}{j\omega L} + j\omega C_2.\tag{4-3}$$

From equations (4-1) and (4-2), the values of L and C_2 are obtained,

$$L = \frac{Z_0 \sqrt{2}}{2\omega}. \qquad (4\text{-}4)$$

$$C_2 = \frac{\sqrt{2}-1}{Z_0 \omega}. \qquad (4\text{-}5)$$

By substituting the frequency ω into equations (4-4) and (4-5), the values of C_1, C_2 and L can be easily calculated. In this work, C_1 was calculated to be 27 pf, C_2 was calculated to be 11 pf, and L was calculated to be 47 nH. The hybrid coupler was built on a PCB from Clinical MR Solutions. Inductors were winded on bench and tested using the network analyzer to verify its value. Figure 4.8 showed a picture of the hybrid.
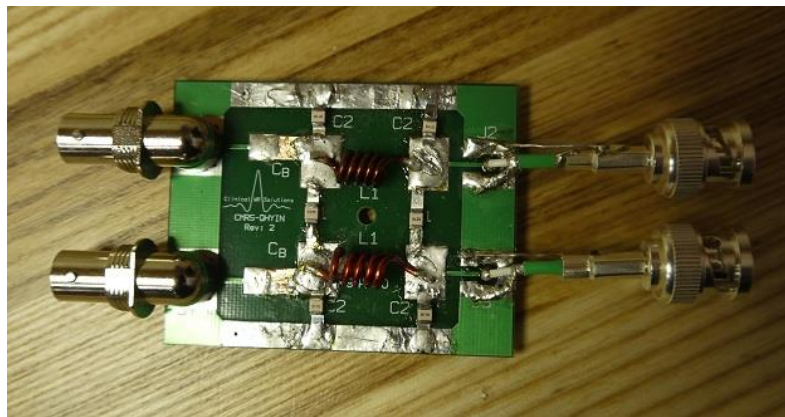
Figure 4.8 Completed lumped elements $\lambda / 8$ hybrid coupler.

The hybrid coupler was tested on the bench using an Agilent 5000 oscilloscope and the HP 8751A network analyzer. Port 1 (Tx port) of the hybrid was connected to port 1 of the network analyzer, the two output ports, Port 2 and Port 3, were connected to two input channels of the oscilloscope, respectively. The input impedances of the oscilloscope had been previously set to 50 Ω. And Port 4 (Rx port) of the hybrid was connected to port 2 of the network analyzer. By doing a S21 measurement and setting the central frequency to 120.15MHz with a 0Hz span, we obtained two signals on the oscilloscope, having the same amplitude and a 90-degree phase shift, as showed in the Figure 4.9.

It is desired to achieve a good isolation between port 1 (Tx) and port4 (Rx) to provide protection to the pre-amplifier during the excitation. The isolation between these two ports was measured with the same configuration, and the span of the network analyzer was set to

20MHz. From the test result we obtained an isolation of -36dB between the Tx port and Rx port at the resonance frequency of 120.15MHz.
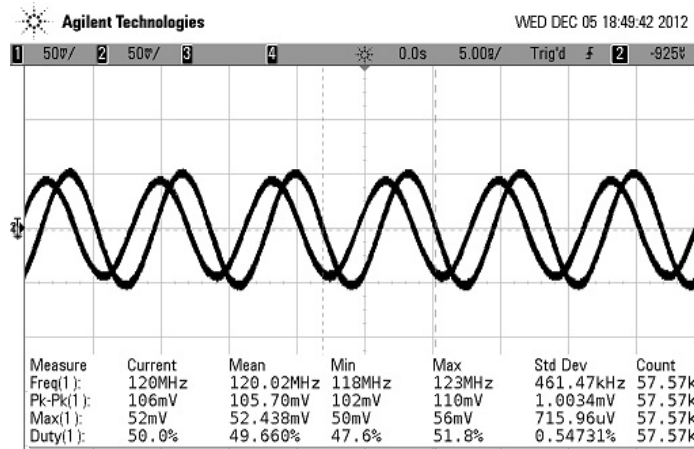
Figure 4.9 A 90-degree phase shift observed at the two output ports of the $\lambda / 8$ hybrid.
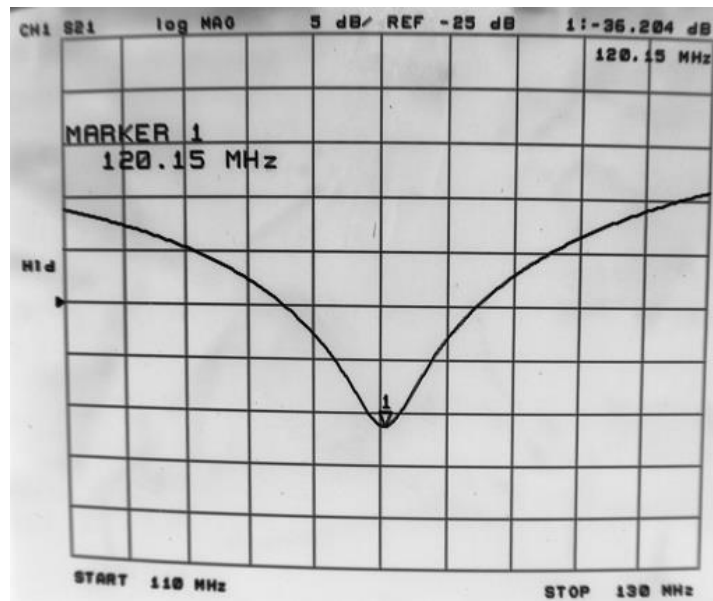
Figure 4.10 S21 response between the port1 and port 4 of the hybrid. An isolation of -36dB was achieved at the frequency of 120.15MHz.

4.5 Results

The performance of the coil was firstly evaluated on the bench by the measuring the matched impedance and Q factor for both the two channels. With a saline bag set inside the coil to mimic the load of a real rat, the impedances of the two channels were matched to 50+j6 ohm and 47+j2 ohm, and the S11 responses obtained are -24dB and -27dB, respectively. The

loaded Q factors of each channel were measured through S11 response, and the Q of the two channels were calculated to be 130 and 136.

To further evaluate the performance of the ^{19}F quadrature birdcage coil in actual NMR experiments, a series of MR spectroscopic and imaging scans were performed on a Philips Achieva 3T scanner in a well-RF-shielded scanner room. A 500ml saline bag was set in the loading position to mimic the load of a rat during the phantom scans, and the S11 response of both the two input ports were measured and finely tuned on the network analyzer after the coil was put into the magnet bore. The coil was calibrated prior to all the scans by doing a several multi-flip-angle spectroscopic scans and adjusting the scanner power output, to perform a true 90-degree excitation pulse.

4.5.1 Phantom spectroscopic scan results

A ^{19}F phantom was made by sealing 5ml Perfluoropropane (PFP) gas into a 5ml syringe. When performing the scans, the syringe was held by a hollow cylindrical foam which was placed in the middle of the coil, to keep it in a region where the homogeneous B_1 field was generated.

Single voxel (SV) spectroscopic scans were performed with the coil on both linear and quadrature modes in order to measure the SNR improvement. To configure the coil for the linear mode, one of the input ports was connected to a 50ohm terminal, while the other one was directly connected to a linear transmit / receive switch. A non-selective sequence was performed with TR of 131ms and TE of 0.14ms. The power required to generate a 90-degree pulse of the same pulse length and the calculated SNR of the received FID signals for each mode are shown the in table 4.2.

<div align="center">

Table 4.2 Comparison of the SNR and power consumption

Coil mode	RF Pulse length	Amplifier Power Output	Calculated SNR
	(us)	(watt)	-
Linear	89	338	110
Quadrature	89	162	156

</div>

In the result, the power required to generate 90-degree pulse of 89us length is 48% less than that of the linear reference. Meanwhile, the SNR of the signal obtained in quadrature mode

is approximately 1.4 times higher than the linear signal reference, which agreed with the calculation and presents an improvement of a factor of square root two. The FID and spectrum results from linear mode and quadrature mode are shown in Figure 4.11.

(a)

(b)

(c)

(d)
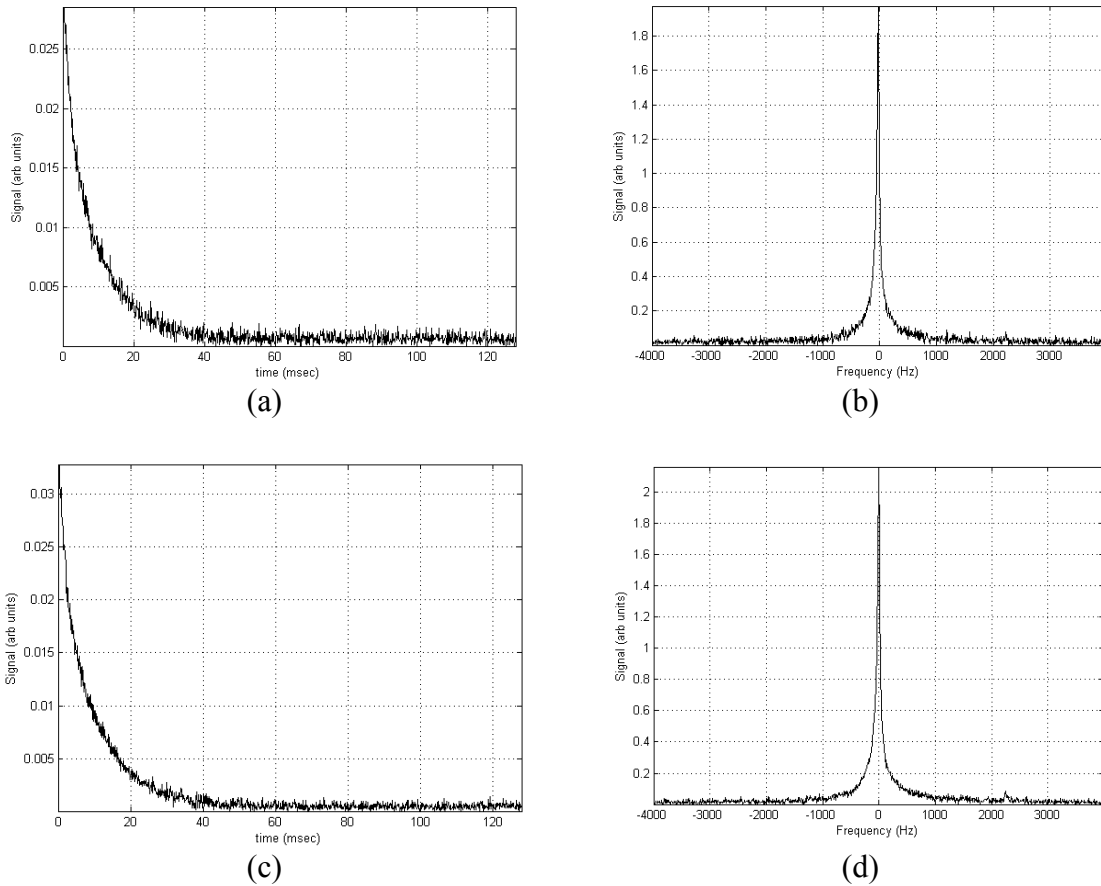
Figure 4.11 FID signal (a) and spectrum response (b) for the coil in linear mode, and FID signal (c) and spectrum response (d) for the coil in quadrature mode.

4.5.2 Phantom imaging scan results

Imaging scans of the phantom were also performed using the constructed quadrature birdcage coil. A 2D FFE sequence was used to acquire transverse and coronal images. For the transverse image, the FOV is 50mm by 50mm, resolution is 128 by 128, TR = 150ms, TE = 3.1ms, 4 signal averages, bandwidth is 200Hz / pixel, and the measured SNR of the image is 16.6. For the coronal image, the FOV is 100mm by 100mm, resolution is 128 by 128, TR = 150ms, TE = 1.7ms, 16 signal averages, bandwidth is 200Hz / pixel, and the measured SNR of the image is 12. The transverse and coronal images are shown in Figure 4.12. In the

49

coronal image, a ghost can be observed, this is resulted from the chemical shift of the PFP gas due to its two intrinsic responses in the NMR spectrum that are approximate 48ppm away from each other.
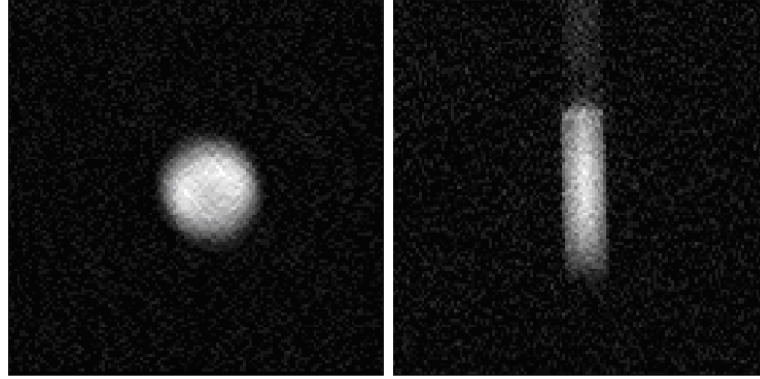
Figure 4.12 Transverse (a) and coronal (b) images of the PFP gas phantom.

4.5.3 B_1 field mapping and field inhomogeneity calculation

As described above, one of the most essential performance measures of a transmit coil is the B_1 field homogeneity. There are several NMR techniques that can be used to quantitatively measure and mapping the B_1 field [27-29]. In this work, a technique called double angle method (DAM) [30, 31] was used. With this method, two RF pulses are applied to excite the magnetization to a flip angle of α and 2α, respectively. When set a long repetition time (TR >> T_1) between the two scans, the two acquired FID signals S_1 and S_2 can be considered independent of relaxation times, and only proportional to sin α:

$$S_1 \propto M_{xy1} = M_0 \sin\alpha \text{,} \tag{4-6}$$

$$S_2 \propto M_{xy2} = M_0 \sin 2\alpha \text{.} \tag{4-7}$$

By combining the equation (4-6) and (4-7), one obtains the value of α;

$$\alpha = \arccos(\frac{S_2}{2S_1}) \text{.} \tag{4-8}$$

It should be noticed that the above calculation is based on the assumptions that the durations of RF pulses are significantly smaller than T_1 and T_2, so the relaxation terms in the Bloch

50

equations can be ignored, and that M_0 is constant during the RF pulse. These are known true for small flip angles, and work well for a flip angle up to 90 degree [32]. At a small flip angle, $B_1 \propto \alpha$, thus by calculating and generating flip angle maps, one can evaluate the field homogeneity of the coil. The limit of this method is that it is inherently slow, since the TR must be long enough to ensure a full relaxation of magnetization between the two flip angles. This may result in a very long scan time, especially in the case of long T_1 nucleus.

A balloon filled up with pure SF_6 gas was put into the coil to create a homogeneous spin system inside the coil. The B_1 mapping scan was performed on a 20mm-thick slice at the center of the coil in the axial direction for the test, with α of 45 degree and 2α of 90 degree. The repetition time TR was set to be 166ms, comparing to that the T_1 of pure SF_6 under 1 atm is about 2ms [33]. This assures a full recovery of the longitudinal magnetization, and thus an accurate calculation results. The full normalized B_1 map of the ^{19}F birdcage coil is shown in Figure 4.13. A plot of the normalized B_1 field of a selected center slice was shown in Figure 4.14.
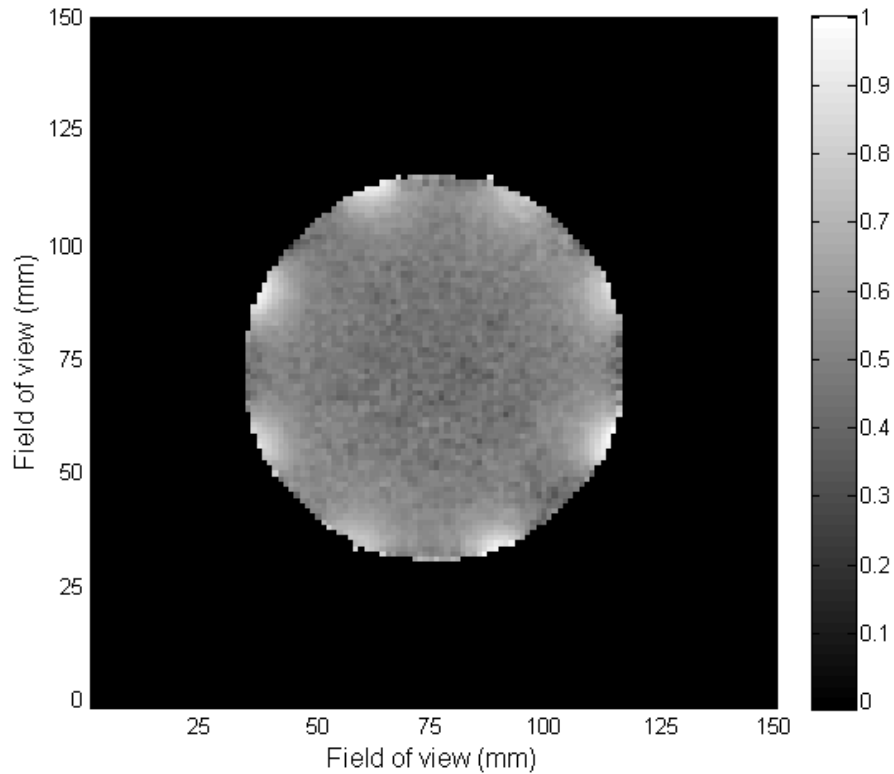
Figure 4.13 Normalized B_1 map of a transverse slice at the center of the coil.

51
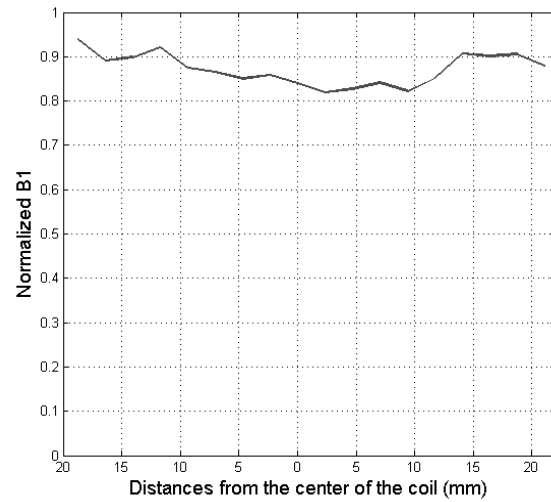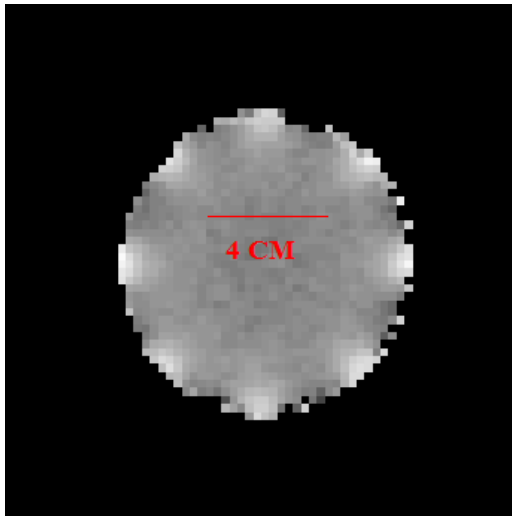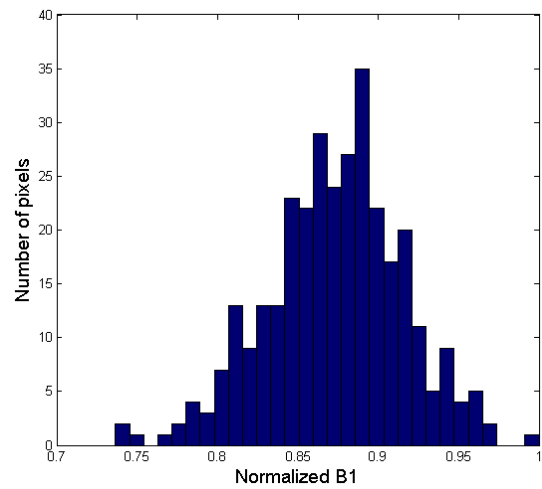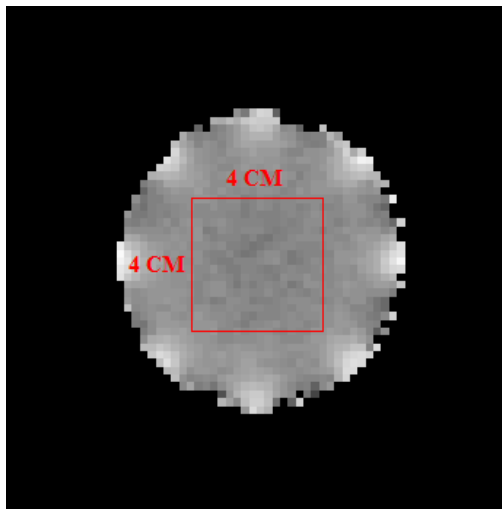
Figure 4.14 (a) Normalized B_1 field distribution in one slice of the map (4 cm), and (b) histogram of the normalized B_1 field throughout the center region of the coil (4 cm * 4 cm).

A 4 cm * 4 cm * 3 cm region at the center of the coil, where the lungs of the rat will be maintained during the experiments, was chosen for quantitative inhomogeneity study. The average normalized B_1 throughout the entire region was calculated to be 0.8731, with a

standard deviation of 0.0426. Therefore the variation of the B_1 field strength at the center region of the coil is about 4.9%.

4.5.4 Animal *in vivo* scan results

Rat *in vivo* lung imaging experiments were performed on a healthy rat using the Philips 3T Achieva scanner. During the experiment, perfluoropropane (PFP) gas mixed with O_2 was delivered to the rat through a custom-built small animal ventilator. All the images were acquired during 17 minutes of continuous breathing of the PFP / O2 mixture.
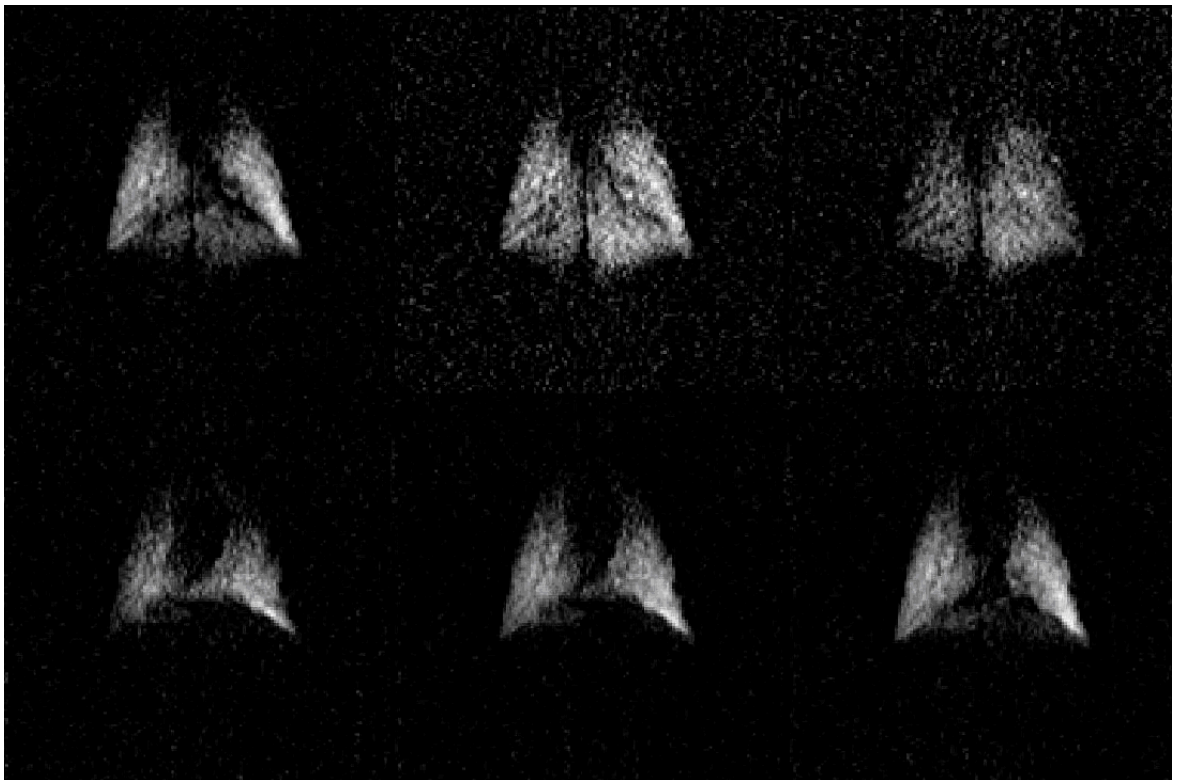
Figure 4.15 Multi-slice images acquired in a healthy rat lung using 3D FFE sequence. FOV = 90*90 mm, Slice thickness = 10mm, TR / TE = 20 / 1.94 ms, NSA = 150.

4.6 Discussion

As transmit / receive coil, the two essential performances, the transmitting field homogeneity and coil sensitivity were quantitatively evaluated. The spectroscopy scan results proved a sensitivity and SNR improvement of a factor of square root two obtained from a quadrature-driven structure, and meanwhile, the power required to excite the spin magnetization has been halved. These improvements agreed very well with the quadrature-driving theory.

In order to evaluate the field homogeneity of the coil, two conventional techniques for B_1 field mapping were studied and investigated. Based on the intrinsic NMR characteristics of the ^{19}F nuclei, that it has a very short T_1 relaxation time, the dual flip angle method (DAM) was chosen to provide a more accurate map and an easier experiment implementation. Pulse sequences parameters were adjusted based on the flip angle calibration results. From the acquired B_1 map, a homogeneous B_1 field distribution was obtained at the center region of the coil.

During the *in vivo* rat lung imaging experiment, the coil has shown very good suitability regarding the dimensions and filling factor. A rat was kept inside the coil where its lung stayed in the center region within the most homogeneous field. Though a volume coil normally has a lower SNR compared to that from a proper sized and positioned surface coil, the diameter of the ^{19}F birdcage coil was set to maximize the filling factor and thus resulted in an optimized SNR.

CHAPTER 5 ^{1}H - ^{129}Xe DOUBLE-BIRDCAGE COIL

5.1 Introduction

Hyperpolarized noble gases MRI using ^{3}He and ^{129}Xe have emerged as promising lung imaging modalities that can provide pulmonary structural and functional. Although ^{3}He can achieve a higher polarization and thus higher signal intensity, its usage and transfer to clinical application are drastically limited for its natural scarcity and high cost. On the other hand, despite the lower polarization, ^{129}Xe has been widely studied and used as an alternative imaging contrast for its abundance [34, 35]. Moreover, xenon is soluble in blood [36] and can be taken into other organs, such as the brain, and gives possibilities to carry out imaging and localized spectroscopy scans in these regions, and obtains functional information. In addition, ^{129}Xe has a chemical shift of 202 ppm in NMR spectrum, which makes it a useful tool to detect the local chemical environment [37-39].

In many ^{129}Xe MRI experiments, coils are expected to provide the abilities of exciting / receiving for both proton and xenon nuclei. For example, in localized spectroscopy scans, proton images are usually required for localization. And more generally, a proton channel is preferred for shimming purpose. This can be best done by either a dual-tune coil [40, 41] which can work at both proton and xenon frequencies, or a switch-tuned coil, whose resonant frequencies can be switched between proton and other nuclei. In this way one ensures identical field profile and filling factor for both frequencies. Nevertheless, one can also adopt two separate coils that are tuned to different frequencies to work in close proximity and obtain a dual-frequency structure [42, 43], especially when the two frequencies are relatively far from each other.

In this chapter, a double-birdcage coil developed and constructed to work at both proton and xenon frequencies is discussed. Double-Birdcage Structure

5.1.1 ^{1}H and ^{129}Xe birdcage coils construction

Two linear high-pass birdcage coils were made separately using the same acrylic tube and copper tape as described in the previous chapter. One coil was tuned to 35.33MHz for xenon

frequency, and the other one was tuned to 127.74 MHz for proton frequency. The two coils were made in different sizes in order to implement the double-birdcage structure. The dimensions of these two coils are shown in table 5.1 and 5.2, respectively. The xenon coil was made the same size with the ^{19}F coil, in order to optimize the filling factor when an experimental subject (such as a rat) is put in. For the proton coil, because of the larger diameter required for the double-birdcage structure, it inevitably has a poorer filling factor, compared to that of the inner xenon coil. Though this can be easily compensated by the high intensity of proton signal, it is made as small as possible, not only to maximize the filling factor, but also to minimize the coupling issue with the proton quadrature body coil (QBC) that is integrated in the scanner.

On the other hand, the mutual inductance between the rungs of the two coils become larger as the diameter of the proton coil decreases and the distance between the two rungs gets smaller. As described in Chapter 2, the resonant modes of a birdcage coil are determined by the ratio of the impedance of the eng-ring segment and that of the rung. Thus when the effective inductance of the rung is changed due to the mutual inductance, the resonant modes of both xenon and proton coil will shift in the spectrum. The same also applies to the end-ring, however, it is rather feasible to make the proton coil long enough to keep a sufficient distance between the two end-rings to minimize the mutual inductance, without jeopardizing a suitable coil dimension for rats. The two coils need to be re-tuned to retain the desired resonant frequencies once they are put together. Decoupling between the two coils will be further discussed in section 5.2.

Table 5.1 ^{129}Xe Inner Birdcage Coil Dimensions

	Material	Length (mm)	Width (mm)	Thickness (mm)	Diameters (mm)
Coil frame	Acrylic tube	128	-	3.25	83.5
End-rings	Copper tape	-	6.5	0.06	90
Rungs	Copper tape	81.5	6.5	0.06	-

Table 5.2 ^{1}H Outer Birdcage Coil Dimensions

	Material	Length (mm)	Width (mm)	Thickness (mm)	Diameters (mm)
Coil frame	Acrylic tube	130	-	3.25	95.5
End-rings	Copper tape	-	6.5	0.06	102
Rungs	Copper tape	110	6.5	0.06	-

The tuning capacitor values were calculated for both coils using the BirdcageBuilder software. For the xenon coil, the tuning capacitor on the end-ring segment is 500 pf, for the proton coil, the tuning capacitor on the end-ring segment is 31.5 pf. Impedance matching was performed using the lumped elements Balun circuit on each coil, the same as described in Chapter 4. Both the two coils were tested on the bench individually before implementing the double-birdcage structure. The S11 responses for the two coils are shown in Figure 5.1.
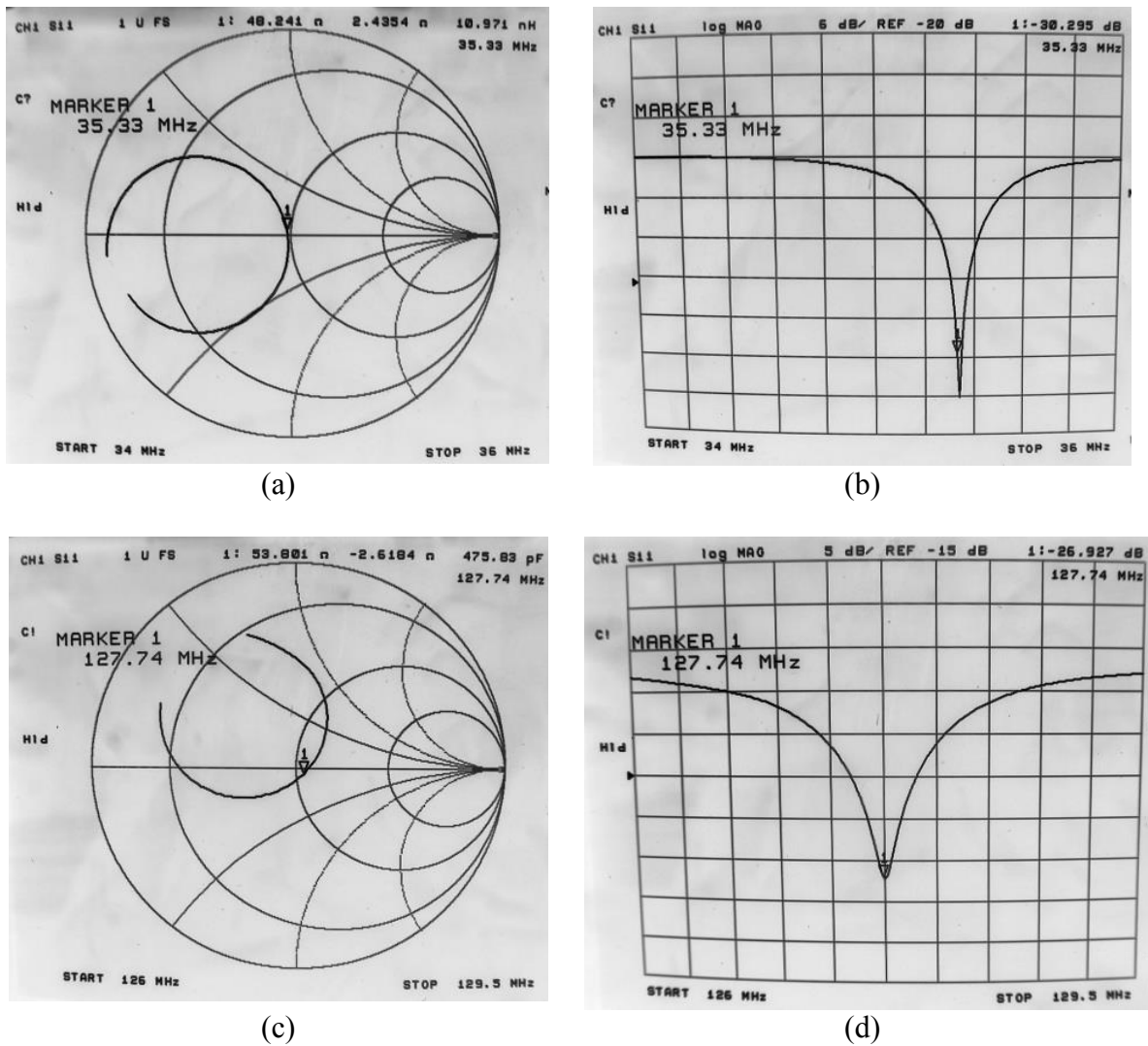

(a)   (b)

(c)   (d)

Figure 5.1 S11 responses of the xenon coil (a) (b) and the proton coil (c) (d).

5.1.2 Double-birdcage structure and coils re-tuning

The double-birdcage structure was constructed by setting the xenon coil in the middle of the proton birdcage coil in such a way that the two coil frames are kept concentric, as shown in Figure 5.2. As discussed above, the proton coil was made as small as possible to achieve the best possible filling factor. This resulted in a limited space inside for the xenon coil. Thus, the Balun matching circuit of the xenon coil was set on the inner surface of the frame, while that of the proton coil was maintained outside its frame.

The resonance mode for each coil was re-tested after the double-birdcage structure had been implemented. A resonance frequency shift was observed in both the xenon and the proton coil. In the xenon coil, the resonance frequency moved from 35.33MHz to 37.5MHz, whilst in the proton frequency it moved farther from 127.7MHz to 116MHz. These resonance frequency shifts result from the mutual inductance between the rungs of the two coils, introduced by their close proximity, which changes the rung effective inductance and hence the impedance. Though the same will also happen between the end-rings of the two coils, it has been reduced to negligibly small by separating the end-rings farther away from each other. Both coils must be re-tuned back to their proper working frequencies. In order to re-tune the proton birdcage coil to the correct frequency, instead of changing the tuning capacitors, the length of the rungs was extended from 8.5cm to 11cm. This extension changed the rung inductance and hence the resonance modes of the proton coil. In addition, it also increases the distance between the end-rings of the two coils, which further decrease the mutual inductance and coupling between them.

At this point, the xenon coil was not fixed to a position but keeping the possibility to rotate inside the proton coil, this helps find out a position for the best geometrically decoupling between the two coils, which will be further discussed in the next section.
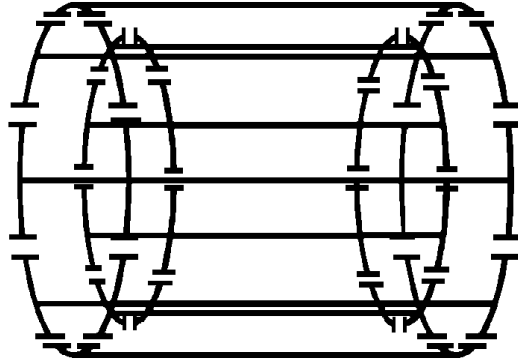
Figure 5.2 Illustrative structure of a double-birdcage coil.

| (a) | (b) |
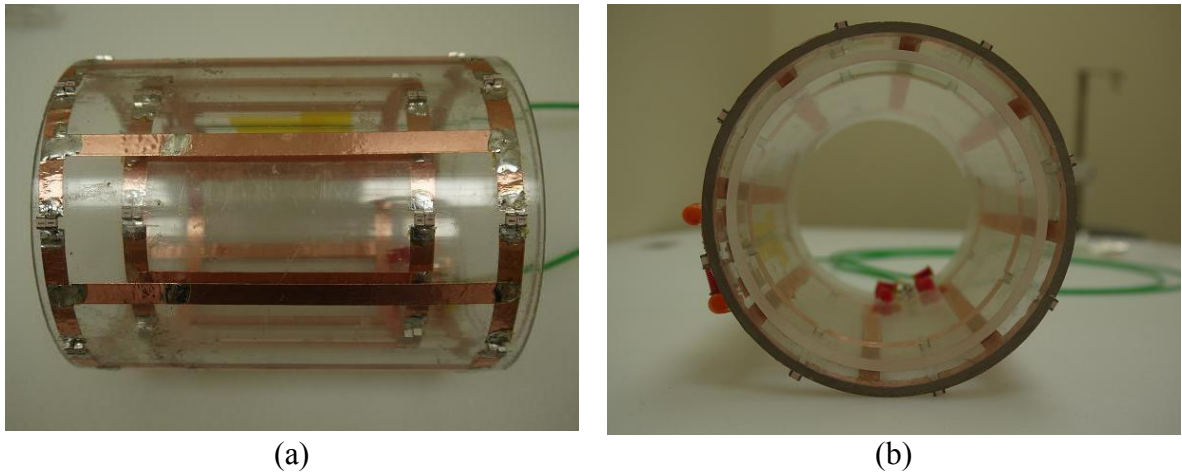
Figure 5.3 Front view (a) and side view (b) of the constructed ^{1}H - ^{129}Xe double-birdcage coil.

5.2 Field Decoupling and Coil Isolation

The field coupling between two adjacent coils should always be handled with care, for its many deleterious effects on both the B_1 field homogeneity and the SNR of the acquired signals. When the coupling exists, during the transmitting, current will be induced in the other coil, which then will create a second magnetic field and conversely distort the main B_1 field. On the other hand, during the receiving, a portion of the electromagnetic energy of the signal will be dissipated in the coupled coil, and thus decrease the SNR by simply reducing the signal intensity. This is especially critical when the two coils are working at close frequencies.

In such cases, active decoupling methods are usually required to achieve the best decoupling performances more effectively. In these methods, one coil is decoupled from another by either shifting its resonance frequency far away from the other, or adding one or multiple RF chocking circuits to the coil to cancel the induced currents. PIN diodes are commonly used to selectively add de-tuning capacitors or chocking inductors to the coil during appropriate periods. In other cases, when the two coils are working at different frequencies that are far away from each other, the coupling between the two becomes less severe. At a cost of decoupling performance, the active decoupling circuits may be omitted for an easier implementation, and the two coils are decoupled geometrically to gain an acceptable isolation in between.

In the double-birdcage structure, the two coils are working at two frequencies of 35.33MHz and 127.74MHz. The distance between their resonance frequencies implies the possibility of geometrically decoupling method. As previously discussed in Chapter 4, a linearly driven birdcage coil creates a linear polarized magnet field in a plane perpendicular to the coil's end-ring plane. Hence, the coupling between two birdcage coils can be possibly minimized when they are placed in such a position where their magnet fields are orthogonal to each other. With the advantage of a concentric structure, it is possible to do quantitative adjustment and measurement to find the positions for a minimized decoupling and optimized isolation.

The xenon birdcage coil was rotated counter clockwise regarding the proton birdcage coil, starting at a position where both the feeding ports of the two coils are at 6 o'clock position, and proceed with a step of $\pi / 8$ degree. To measure the isolation between the two coils, the xenon coil and proton coil were connected to port 1 and port 2 of the network analyzer, respectively. At a transmitting frequency of xenon (35.33MHz), the S21 parameter was measured for each step. Then, the measurements were repeated again with the two coils switched the ports of the network analyzer, and the transmitting frequency adjusted to that of proton (127.74MHz). The measurements results are shown in the Figure 5.4.
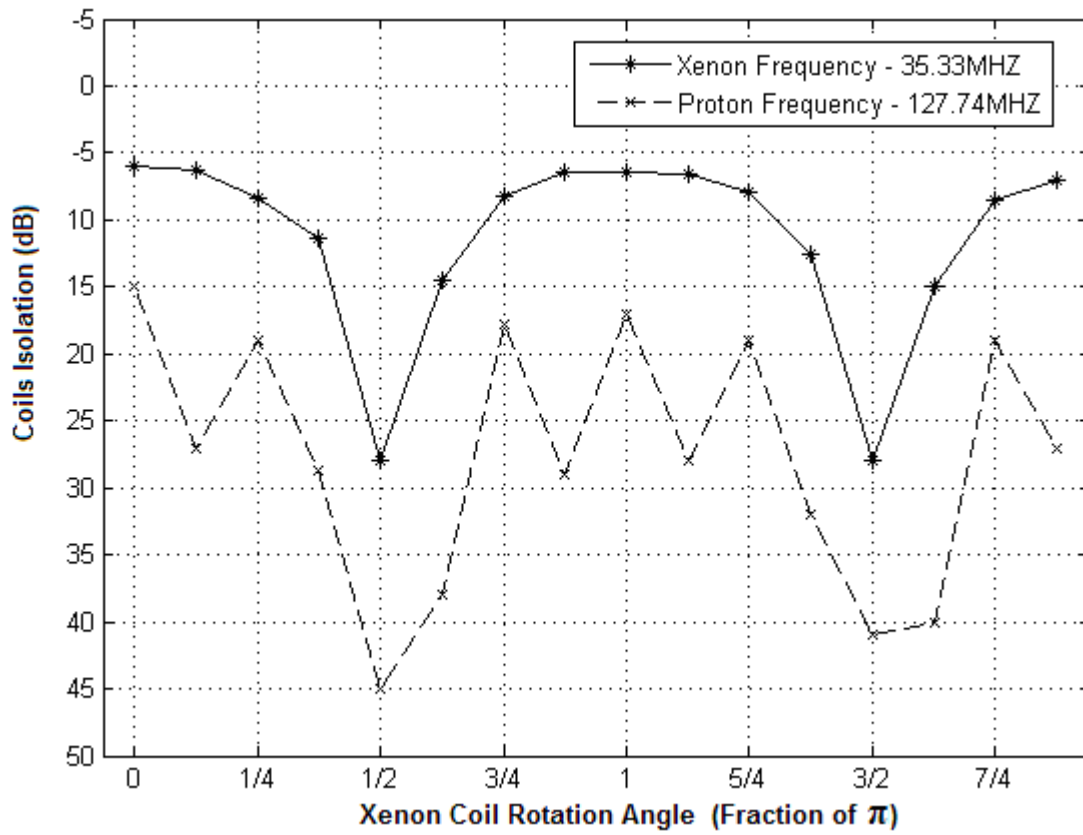
Figure 5.4 Isolation V.S. the relative positions of the two birdcage coils.

From Figure 5.4, the solid line showed the isolation between the two coils when the xenon coil was used as a transmitting coil, and the broken line showed the isolation when the proton coil was used as a transmitting coil. In both situations the isolation between the two coils achieved the optimum when there was a 90 degree between the two feeding ports, indicating that the generated magnetic fields from the two coils are orthogonal to each other, obviously. At xenon frequency of 35.33MHz, the maximum isolation between the two coils had reached 28dB, and at proton frequency of 127.74MHz, it had reached 45dB. These isolations have proved that the two coils are sufficiently electrically decoupled using geometrically decoupling method. Figure 5.5 and Figure 5.6 showed the simultaneous test results of S11 parameter, as impedance matching measurement, and S21 parameter, as coil decoupling measurement, for both xenon coil, and proton coil, respectively.
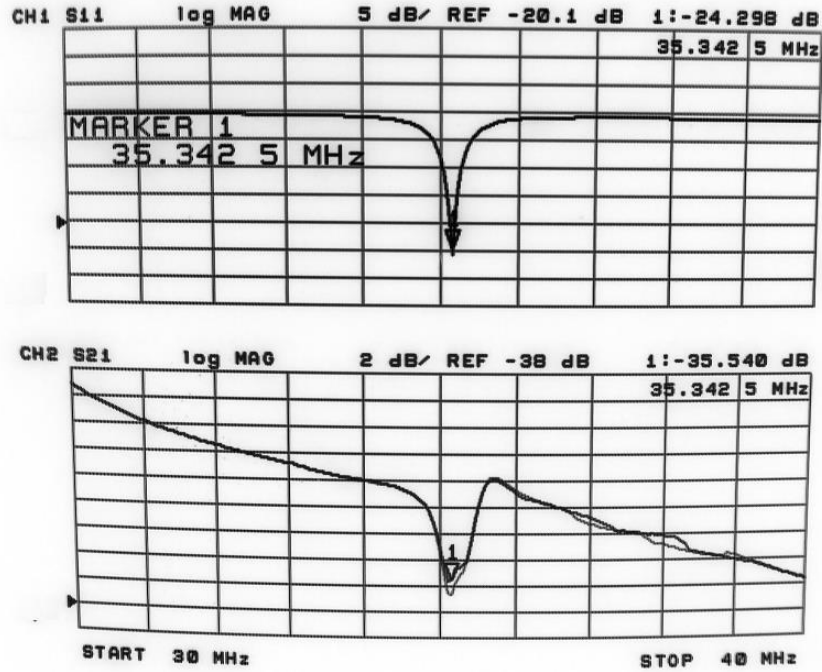
Figure 5.5 S11 response of the xenon coil (a) and S21 response between the xenon and proton coils (b).
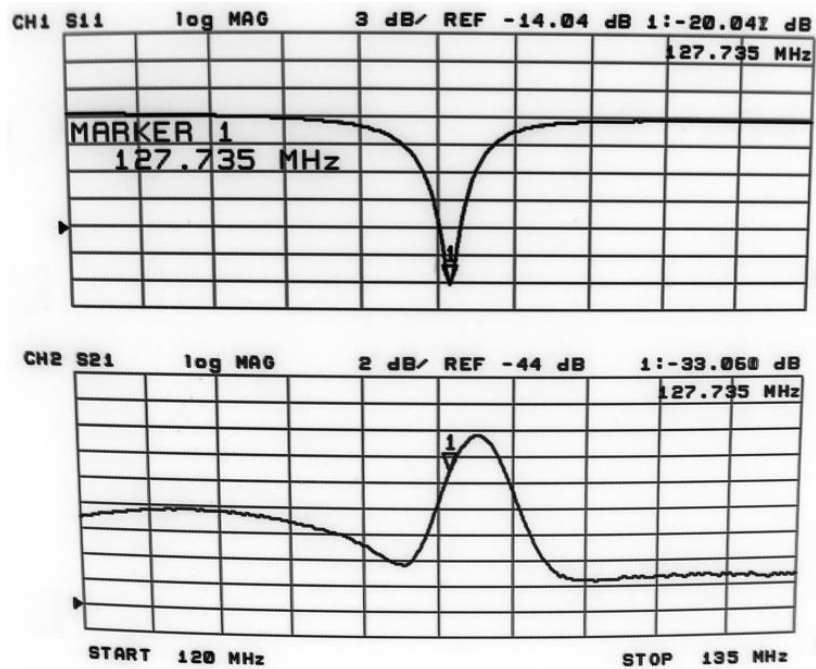

Figure 5.6 S11 response of the proton coil (a), and S21 response between the proton and xenon coils (b).

5.3 Results

5.3.1 Q factor value

The Q factors of both proton and xenon birdcage coils were measured on the bench before and after the double-birdcage structure was formed, respectively, through the S11 responses. A 500ml saline bag, simulating a real rat, was used to load the coils. When measured separately, the xenon birdcage coil obtained a loaded Q of 104, while the proton birdcage coil had a loaded Q of 91. Subsequently, the xenon coil was set into the proton coil and the loaded Q values of the two coils were measured again. In the double-birdcage structure, the xenon and proton coils obtained a loaded Q of 106 and 95, respectively. From the values we can see clearly that the Q factors of both the two coils maintained about the same value after they were put together and form the double-birdcage structure. In other words, the sensitivities of the two coils are not affected by forming the double-birdcage structure.

5.3.2 Imaging scan results and image registration

In order to test and verify the xenon / proton dual-frequency imaging ability of the double-birdcage coil, phantoms imaging experiments were performed using a glass ball of thermal-polarized xenon phantom and a 5ml saline syringe proton phantom, as shown in Figure5.8a. The xenon and proton phantoms are placed inside the double-birdcage coil, as shown in Figure 5.8b, to simulate a real rat lung imaging scan, when xenon images will be acquired from the lung and proton images are acquired to obtain the anatomical structure of the body.
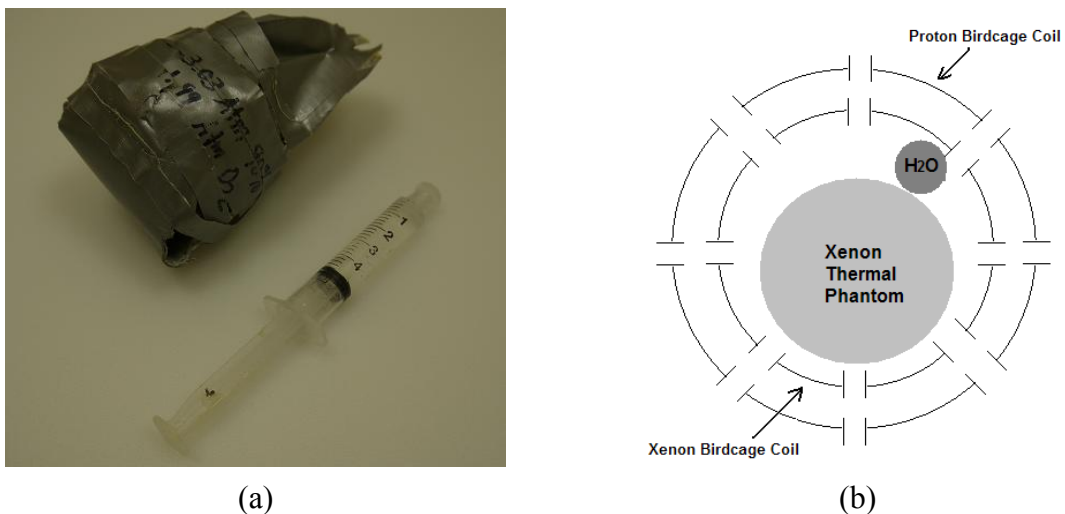

(a)   (b)

Figure 5.7 Xenon thermal phantom and saline syringe phantom (a) are set up inside the coil (b).

Scans were performed on the Philips Achieva 3T scanner. The two birdcage coils are interfaced to the scanner via a commercially purchased Dual Frequency Gateway (DFG) interface device from Clinical MR Solution. Firstly, the proton images were acquired using a FFE sequence for both transverse and coronal views. Subsequently, without moving the coil and the phantoms, the xenon images were acquired as well. Scan parameters are listed in the table 5.4.

Table 5.3 Scan parameters and results

Nuclei	Sequence	View	FOV (mm)	Resolution	TR / TE (ms)	Slice Thickness (mm)	Average	SNR
^{1}H	FFE	Transverse	150*150	128*128	150/1.24	5	1	21.5
^{1}H	FFE	Coronal	150*150	128*128	150/1.12	5	1	39
^{129}Xe	FFE	Transverse	150*150	64*64	250/5	300	16	6.5
^{129}Xe	FFE	Coronal	150*150	64*64	250/5	300	16	7.2

From the proton and xenon image results, image registration post processing was performed in Matlab. Two images (transverse view and coronal view) were generated with the proton image registered on the xenon image. Since during the two different nucleus scans, the subject had not been moved, and the sequences were deliberately set to have the same FOV and matrix size, these registration images reveals the true spatial structural information with great accuracy between the two phantoms, which will be of great use in the case of *in vivo* animal studies.
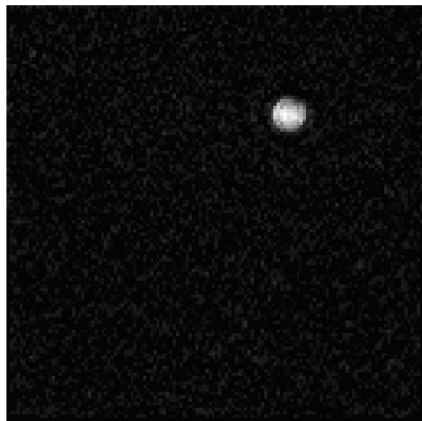
(a)
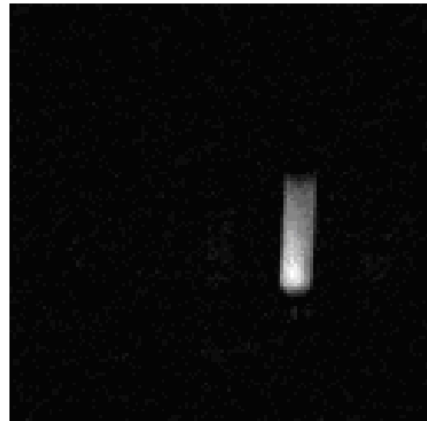
(b)
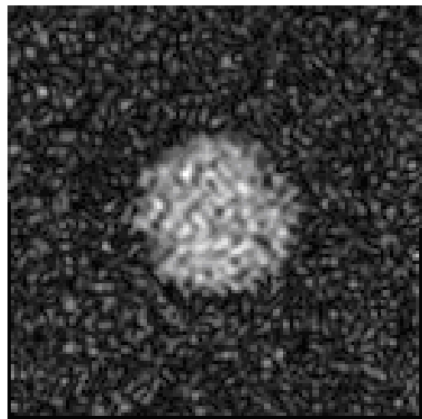
(c)

(d)

(e)

(f)

Figure 5.8 Transverse (a) and coronal (b) images of the saline syringe phantom; transverse (c) and coronal (d) images of the xenon thermal phantom; and transverse (e) and coronal (f) registered images of xenon and proton.

5.4 Discussion

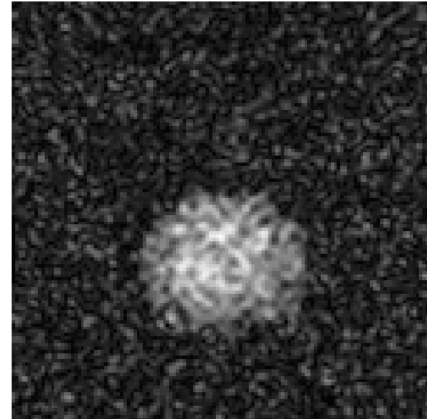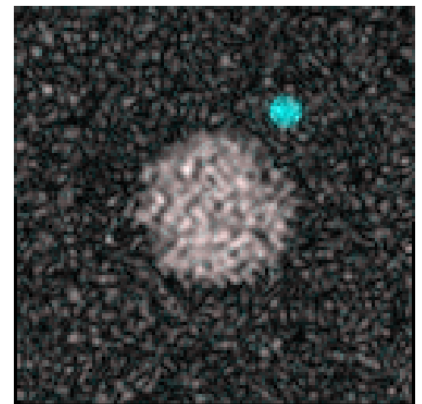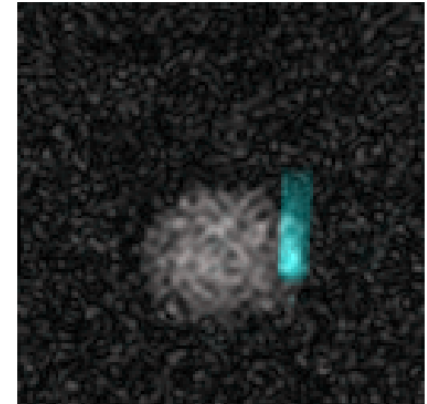The key part of the double-birdcage coil design is the decoupling between the two individual coils. Unlike that between a transmit-only coil and a receive-only coil, which always adopts an active decoupling method using PIN diodes, the decoupling between these coils is solely achieved by geometry. This is possible because of the resonance frequencies of the two coils are distant from each other. From the measurement results, a maximum isolation of 40dB was obtained at the proton frequencies, while at xenon frequency, the maximum isolation achieved was 28dB. This difference possibly results from the fact that both birdcage coils have a high-pass structure, meaning they both have three other resonance modes of which the frequencies are lower than that they're currently working at. During the proton transmitting, the proton frequency of 127.74MHz is far away from the xenon frequency of 35.33MHz, which is the highest resonance frequency of the xenon coil, thus very small coupling occurred. However, when the xenon coil is transmitting a pulse of 35.33MHz, one of the resonance modes of proton birdcage coil has a resonant frequency close to it, thus part of the signal was picked up by the proton birdcage coil, and it degrades the isolation between the two coils. Nevertheless, the isolations between the two coils at both proton and xenon frequencies are sufficiently high to eliminate the coupling effects from the image quality, and to assure the ability of double-frequency scan without relocating the subject for this coil structure.

It hasn't been possible to do an experiment with hyperpolarized xenon gas, due to the unfinished polarizer installation in the facility. Scans with the thermal xenon phantom were performed and results were compared with that from a previously made, single linear xenon birdcage coil. The SNR of the signal from the double birdcage coil is 7, lower than that of 9 from the single linear birdcage coil. This difference mainly resulted from the increased noise that was introduced by the presence of the proton birdcage coil, as well as possible distortion of the xenon B_1 field, due to the imperfect isolation between the two coils. Besides, the thermal xenon phantom couldn't provide signal good enough to perform an accurate B_1 mapping scan, this will be done after the xenon polarizer is ready and hyperpolarized xenon gas is available.

In the future work, in order to overcome the issue of decreased SNR in the double birdcage coil, further investigation on the possibility of a quadrature-driven structure implementation on the xenon birdcage coil will be conducted. As described in Chapter 4, a quadrature-driven mode will increase the SNR by a factor of square root of two. This will compensate the SNR loss in a double-birdcage coil. However, a quadrature-driven coil will develop a circularly polarized B_1 field, which makes it impossible to keep the two B_1 field orthogonal all the time, thus will greatly degrade the isolation between the two coils. In this case, an active decoupling method might be required.

After the work in this thesis had been finished, the xenon coil was taken outside the proton birdcage coil and was modified temporarily to a quadrature-driven mode, to evaluate the performance in a normal *in vivo* rat scan. Chemical-shift spectroscopic scans were performed using hyperpolarized xenon gas in a healthy rat, and results are shown in Fig5.9.
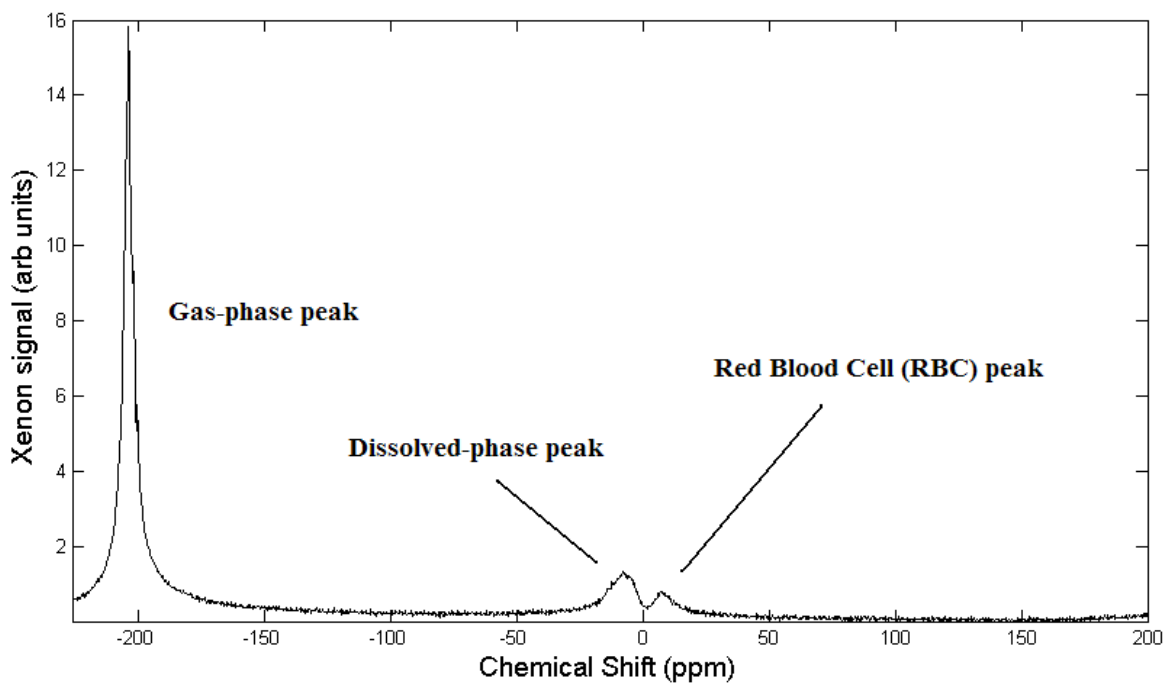
Figure 5.9 In vivo chemical-shift spectrum obtained from a health rat using the quadrature-driven xenon birdcage coil.

67

CHAPTER 6 CONCLUSION

Firstly, a quadrature birdcage coil was developed to work at ^{19}F frequency under 3T magnetic field. It was optimized to suit *in vivo* rat lung imaging experiments using inert fluorinated gases. Compared to the linear reference, coil sensitivity was improved by a factor of 1.4, and power consumption was halved with the quadrature structure. The transmit B_1 field distribution was quantitatively investigated using Dual Angle Method (DAM), and a homogeneous B_1 map was obtained at the center of the coil. *In vivo* rat lung imaging experiments were performed using inert fluorinated gas, and multi-slices lung images of the rat were obtained.

Secondly, a ^{1}H - ^{129}Xe double-birdcage coil was developed to provide the deal-frequency imaging ability without having to re-configure the coil or relocating the experimental subject. The decoupling between the two birdcage coils was quantitatively investigated. With geometrically decoupling, an isolation of 28dB was obtained at xenon frequency, and an isolation of 45dB was obtained at proton frequency. Images were acquired from both xenon and proton phantoms, and images registration processing was able to be performed accurately.

In order to further improve the SNR for the two sets of coils, RF shielding will be constructed and applied to both sets of coils in future work. Also, the B_1 mapping tests will be performed on the double-birdcage coils using hyperpolarized xenon gas, to quantitatively evaluate the B_1 field homogeneity, and distortion resulted from the coupling between the two coils.

REFERENCES

[1] E. M. Purcell, H. C. Torrey, and R. V. Pound. Resonance absorption by nuclear magnetic moments in a solid. *Physical Review*, 69:37–38, 1946.

[2] F. Bloch. Nuclear induction. *Physical Review*, 70:460–474, 1946.

[3] P. C. Lauterbur. Image formation by induced local interactions: Examples employing nuclear magnetic resonance. *Nature*, 242:190–191, 1973.

[4] P. Mansfield and P. K. Grannell. NMR 'diffraction' in solids? *Journal of Physics C: Solid State Physics*, 6:L422–426, 1973.

[5] Albert, M.S. et al. (1994) Biological magnetic resonance imaging using laser polarized 129Xe. Nature, 370, 199-201.

[6] Kuethe DO, Caprihan A, Fukushima E, Waggoner RA. Imaging lungs using inert fluorinated gases. Magn Reson Med 1998; 39: 85-88.

[7] Soher BJ, Ainslie M, MacFall J, Hashoian R, Charles HC, editors. Lung Imaging in Humans at 3T using Perfluorinated Gases as MR Contrast Agents. *Proceedings of the 18th Annual Meeting ISMRM*; 2010; Stockholm, Sweden.

[8] Kuethe DO, Caprihan A, Fukushima E, Waggoner RA. Imaging lungs using inert fluorinated gases. *Magn Reson Med*. 1998; 39(1):85-8.

[9] Schreiber WG, Eberle B, Laukemper-Ostendorf S, Markstaller K, Weiler N, Scholz A, et al. Dynamic 19F-MRI of pulmonary ventilation using sulfur hexafluoride (SF6) gas. *Magn Reson Med*. 2001;45(4):605-13.

[10] Kuethe DO, Behr VC, Begay S. Volume of rat lungs measured throughout the respiratory cycle using 19F NMR of the inert gas SF6. *Magn Reson Med*. 2002; 48(3):547-9.

[11] Adolphi NL, Kuethe DO. Quantitative mapping of ventilation-perfusion ratios in lungs by 19F MR imaging of T1 of inert fluorinated gases. *Magn Reson Med*. 2008; 59(4):739-46.

[12] D. I. Hoult. The principle of reciprocity in signal strength calculations: a mathematical guide. *Conc. Magn. Reson.,* 12(4):173-187, 2000.

[13] H.E. Moller, X.J. Chen, M.S. Chawla, B. Driehuys, L.W. Hedlund, and G.A. Johnson. Signal Dynamics in Magnetic Resonance Imaging of the Lung with Hyperpolarized Noble Gases. J. Magn. Reson., 135:133-143, 1998.

[14] J. Mispelter, M. Lupu and A. Briguet, *NMR Probeheads for Biophysical and Biomedical Experiments: theoretical principles and practical guidelines*. Imperial College Press, 2006.

[15] F. D. Doty, Y. A. Yang, and G. E. Entzminger, "Magnetism in NMR Probe Design Part I: General Methods," Concepts in Magn. Resn., Vol 10(3) , 133-156 (1998).

[16] P. B. Roemer, W. A. Edelstein, C. E. Hayes, S. P. Souza, and O. M. Muller. The nmr phase array. *Mag. Reson. Med.,* 16:192-225, 1990.

[17] K. P. Pruessmann, M. Weiger, M. B. Scheidegger, and Peter Boesiger. Sense: Sensitivity encoding for fast mri. *Mag. Reson. Med.,* 42, 1999.

[18] C. E. Hayes et al., "An efficient, highly homogenous radiofrequency coil for whole-body NMR imaging at 1.5 T", *Journal of Magnetic Resonance*, (63): 622-628; 1985.

[19] C.L. Chin and M.B. Smith, "Circular and elliptical birdcage coil design for magnetic resonance imaging", New York: IEEE, 1998.

[20] C. L. Chin et al., "BirdcageBuilder: Design of specified-geometry birdcage coils with desired current pattern and resonance frequency", *Concepts in Magnetic Resonance*, 15(2): 156-163, 2002.

[21] Couch MJ, Ball IK, Li T, Fox MS, Littlefield SL, Biman B, Albert MS. 19F Ultra-Short Echo Time MRI of Human Lungs Using Inert Fluorinated Gases. American Thoracic Society

[22] Jacob RE, Chang YV, Choong CK, Bierhals A, Hu DZ, Yablonskiy DA, Woods JC, Gierada DS, Conradi MS. 19F MR imaging of ventilation and diffusion in excised lungs. *Magn Reson Med* 2005; 54:577–585.

[23] Ruiz-Cabello J, Perez-Sanchez JM, Perez de Alejo R, Rodriguez I, Gonzalez-Mangado N, Peces-Barba G, Cortijo M. Diffusion-weighted 19F-MRI of lung periphery: Influence of pressure and air-SF6 composition on apparent diffusion coefficients. *Resp Physiol Neurobiol* 2005; 148:43–56.

[24] M.C. Leifer, "Resonant modes of the birdcage coil", *Journal of Magnetic Resonance*, vol. 124,(no.1), pp. 51-60, 1997.

[25] N. Chen, D. I. Hoult, and V. I. Sank. Quadrature detection coils – a further improvement in sensitivity. *J. Magn. Reson.,* 54:324-327, 1983.

[26] R. K. Mongia, I.J. Bahl, P. Bhartia, J. Hong. *RF and Microwave Coupled-Line Circuits*. Artech House, Incorporated, 2007.

[27] Oh C, Hilal S, Cho Z, and Mun I. Radio frequency field intensity mapping using a composite spin-echo sequence. *Magn Reson Imaging* 1990; 8:21-25.

[28] Morrell GR. A phase-sensitive method of flip angle mapping. *Magn Reson Med* 2008; 60:889-894.

[29] Sacolick LI, Wiesinger F, Hancu I, and Vogel MW. B1 mapping by Bloch-Siegert shift. *Magn Reson Med* 2010; 63:1315-1322.

[30] Insko E and Bolinger L. Mapping of the radiofrequency field. J *Magn Reson A* 1993; 103:82-85.

[31] Hornak JP, Szumowski J, and Bryant RG. Magnetic field mapping. *Magn Reson Med* 1988; 6:158-163.

[32] Pauly J, Nishimura D, and Macovski A. A k-space analysis of small-tip-angle excitation. *J Magn Reson* 1989; 81:43-56.

[33] Pablo J. Prado; Bruce J. Balcom; Igor V. Mastikhin; Albert R. Cross; Robin L. Armstrong; Alan Logan. Magnetic Resonance Imaging of Gases: A Single-Point Ramped Imaging with T1 Enhancement (SPRITE) Study. *J. Magn. Reson.,* (137): 324-332, 1999

[34] Mata JF, Altes TA, Cai J, Ruppert K, Mitzner W, et al. (2007) Evaluation of emphysema severity and progression in a rabbit model: Comparison of hyperpolarized 3He and 129Xe diffusion MRI with lung morphometry. *J Appl Physiol* 102: 1273–1280.

[35] Driehuys B, Cofer GP, Pollaro J, Mackel JB, Hedlund LW, et al. (2006) Imaging alveolar-capillary gas transfer using hyperpolarized 129Xe MRI. Proc *Natl Acad Sci* U S A 103: 18278–18283.

[36] Chen RYZ, Fan FC, Kim S, Jan KM, Usami S, et al. (1980) Tissue-blood partition-coefficient for xenon: Temperature and hematocrit dependence. *J Appl Physiol* 49: 178–183.

[37] Lowery TJ, Doucleff M, Ruiz EJ, Rubin SM, Pines A, et al. (2005) Distinguishing multiple chemotaxis Y protein conformations with laser-polarized 129Xe NMR. *Protein Sci* 14: 848–855.

[38] Dubois L, Da Silva P, Landon C, Huber JG, Ponchet M, et al. (2004) Probing the hydrophobic cavity of lipid transfer protein from Nicotiana tabacum through xenon-based NMR spectroscopy. *J Am Chem Soc* 126: 15738–15746.

[39] 9. Wolber J, Cherubini A, Leach MO, Bifone A (2000) Hyperpolarized 129Xe NMR as a probe for blood oxygenation. *Magn Reson Med* 43: 491–496.

[40] A. R. Rath, "Design and performance of a double-tuned birdcage coil", *Journal of Magnetic Resonance*, (86): 488-495; 1990.

[41] G. X. Shen et al., "Dual-frequency, dual-quadrature, birdcage RF coil design with identical B1 pattern for sodium and proton imaging of the human brain at 1.5 T", *Magnetic Resonance in Medicine*, (38): 717- 725, 1997.

[42] J.R. Fitzsimmons et al. "Double Resonant quadrature birdcage", *Magnetic Resonance in Medicine (MRM),* (30): 107-114, 1993.

[43] T. Lanz et al., "Double tuned 23Na 1H nuclear magnetic resonance birdcage for application on mice in vivo", *Review of Scientific Instruments*, 72(5): 2508-2510; 2001.